Journal of Nuclear Materials 408 (2011) 209–223

Contents lists available at ScienceDirect

Journal of Nuclear Materials

journal homepage: www.elsevier.com/locate/jnucmat

Modelling of iodine-induced stress corrosion cracking in CANDU fuel

B.J. Lewis [a,*], W.T. Thompson [a], M.R. Kleczek [a], K. Shaheen [a], M. Juhas [a], F.C. Iglesias [b]

[a] Department of Chemistry and Chemical Engineering, Royal Military College of Canada, P.O. Box 17000, Kingston, Ontario, Canada K7K 7B4
[b] Candesco Corporation, 230 Richmond Street, 10th Floor, Toronto, Ontario, Canada M5V 1V6

ARTICLE INFO

Article history:
Received 7 September 2010
Accepted 25 October 2010
Available online 9 November 2010

ABSTRACT

Iodine-induced stress corrosion cracking (I-SCC) is a recognized factor for fuel-element failure in the operation of nuclear reactors requiring the implementation of mitigation measures. I-SCC is believed to depend on certain factors such as iodine concentration, oxide layer type and thickness on the fuel sheath, irradiation history, metallurgical parameters related to sheath like texture and microstructure, and the mechanical properties of zirconium alloys. This work details the development of a thermodynamics and mechanistic treatment accounting for the iodine chemistry and kinetics in the fuel-to-sheath gap and its influence on I-SCC phenomena. The governing transport equations for the model are solved with a finite-element technique using the COMSOL Multiphysics® commercial software platform. Based on this analysis, this study also proposes potential remedies for I-SCC.

1. Introduction

During the operation of a nuclear reactor, iodine-induced stress corrosion cracking (I-SCC) may occur in the zirconium alloy sheathing especially during power-ramping manoeuvres. This process can be attributed to the joint action of fission products, primarily iodine, and mechanical stresses resulting from radiation-induced swelling and thermal expansion of the fuel. The pellet-cladding interaction (PCI) may eventually lead to nucleation and propagation of cracks through wall, which frequently appear close to the pellet interface where fission products concentrate (see Fig. 1) [1,2].

During the early 1970s, occurrence of fuel failures in CANDU fuel at the Pickering and Douglas Point Nuclear Generating Stations was observed during sustained power ramps [3,4]. This led to the development of an improved re-fuelling scheme to minimize the hoop stress in the sheathing during the power ramp manoeuvre, and the introduction of a (chemical) barrier coating of graphite (CANLUB) on the internal surface of the sheath. The search for PCI mitigation, particularly for Boiling Water Reactors, also resulted in the mid 1970s in the development of barrier fuel with a thin, pure zirconium layer on the inside surface of the tubing [3,4]. Consequently, detected current failure rates are typically less than ten per million rods in operation [4].

The dominant variables that affect the I-SCC mechanism include: (i) operational conditions (e.g., pre-ramp fuel power and size of the fuel power ramp, fuel burnup, coolant and sheath temperature, strain and creep rate of the fuel sheathing); and (ii) design details (e.g., pellet shape, fuel cracking and hour-glassing, type of impurities and thickness of the CANLUB interlayer coating, pellet and sheath diameter, fuel stack axial clearance, shape of the re-entrant corner at the sheath/end-cap junction, enrichment resulting in variations in end-flux peaking, and the radial temperature distribution within the pellet). In particular, the fuel element contains several stress concentration locations, including circumferential ridges, sheath/end-cap junctions, junctions of appendages with the sheath, and possibly regions adjacent to radial cracks in the pellets [5]. These factors therefore lead to mechanical drivers for failure, which include: the degree of local multi-axiality of stresses, localization of stress/strain over pellet cracks, and unrelaxed stresses from previous ramps. For instance, the most important strain at circumferential ridges is the increment of total on-power mechanical hoop strain at the circumferential ridge during the power ramp.

A thick oxide initially inhibits I-SCC through a simple barrier effect where there is a compressive stress due to the volume ratio of oxide-to-metal (Pilling–Bedworth ratio) for ZrO_2 [6]. Thus, to initiate SCC failure in the sheath, the ridge strain needs to first break the protective ZrO_2 layer in order to expose the sheath to chemical attack from corrosive fission products. It is expected that the failure strain in the sheath to cause superficial oxide layer cracking is in the range of 0.1–0.5% [7]. The CANLUB layer can increase the threshold for power-ramp defects through speculated chemical reactivity with the corrodent fission products [8]. A critical strain/strain rate is required to exceed the strain-to-failure limit for the given microstructure conditions, fluency, corrodent concentration and sheath temperature. This process is sensitive to the state of the material strength of the

* Corresponding author. Tel.: +1 613 541 6611; fax: +1 613 542 9489.
E-mail address: lewis_b@rmc.ca (B.J. Lewis).

0022-3115/$ - see front matter Crown Copyright © 2010 Published by Elsevier B.V. All rights reserved.
doi:10.1016/j.jnucmat.2010.10.063

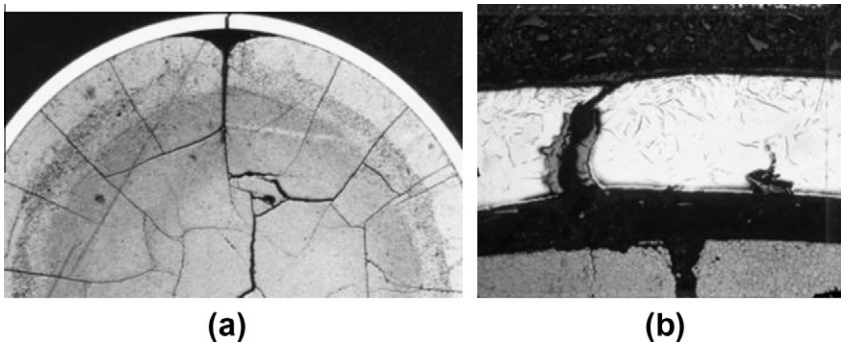

Fig. 1. Ceramograph of an SCC failure with (a) necking of the sheath above a UO_2 crack with localized stresses and (b) crack propagation with shear in the Zircaloy sheath. Courtesy of Atomic Energy of Canada Limited.

sheath. Here I-SCC susceptibility is enhanced by irradiation. In particular, neutrons and fission fragments can induce damage in the sheathing material, where dislocation hoops can form in the Zircaloy metal, i.e., stress-induced clearing of irradiation damage can produce slip steps that intersect the Zircaloy surface [9]. Thus, irradiation-induced hardening, due to the introduction of a large number of point defects, can make the irradiated material more sensitive to SCC with a lower stress threshold with fewer possibilities to deform plastically so as to reduce the applied stress for pseudo-cleavage crack propagation [10,11].

The I-SCC failure mechanism is thought to occur through the following process: (a) the expanding pellet stretches the sheath, resulting in stresses and strains in the sheath during the power ramp; (b) the protective oxide layer at the sheath inner surface breaks; (c) the protective oxide may not be reformed in an intact fuel element since the chemical potential of oxygen may be too low; (d) depending on the prevalent conditions, the sheath can be stretched further and even pass the yield stress; (e) a crack initiates; (f) the incipient crack propagates through the thickness of the sheath with (g) possible final shear failure through the wall. Hence, sheath failure by I-SCC can be described in four stages: (i) crack initiation, (ii) localized intergranular (IG) crack growth, (iii) transgranular (TG) crack propagation, and (iv) final sheath failure [12]. The initiation step is influenced by the oxygen partial pressure, local plastic strain, strain rate, and grain orientation [12]. The IG crack development is particularly influenced by grain orientation/texture, while the TG crack propagation is affected by the stress intensity factor [13]. Fast TG pseudo-cleavage cracking can occur with iodine diffusion to the crack tip due to a weakening of the Zr–Zr bonds that lead to separation along grain boundaries, i.e., this latter process can lead to cracking well below the rupture stress for Zircaloy in an iodine-free environment [14]. In particular, the power ramp will release short-lived fission products adding to the available iodine partial pressure. The iodine-containing compound CsI is found in highest concentration in the fuel-to-sheath gap [15]. Iodine is produced by decomposition of the stable CsI compound that can occur with fission fragment bombardment with a threshold energy for decomposition of 4.35 eV that is much higher than the thermal energy [15]. The iodine released from radiolysis can form $ZrI_{4(g)}$ vapour in regions where the Zr is exposed, which can advance the crack with Zr transport away from the crack tip/pits by a Van Arkel vapour transport mechanism [7,16,17].

The current paper describes an understanding of the thermodynamics in the fuel-to-sheath gap (Section 2) for the development of a mechanistic kinetic model (Section 3) in order to explain the underlying chemistry effects of the I-SCC phenomena.

2. Thermodynamic analysis

Utilizing computational thermodynamic analyses, the chemical destiny of fission products (e.g., iodine) was investigated. This methodology included the use of existing thermodynamic data in FACT (Facility for the Analysis of Chemical Thermodynamics) to describe the equilibrium behaviour of multi-component systems involving customized Gibbs energy functions [18]. The passage of volatiles across the fuel-to-sheath gap is influenced significantly by the partial pressure, i.e., gaseous concentration of the particular volatile fission product. The vapour phase chemistry therefore controls which elements contact the Zircaloy sheath and which are believed to cause I-SCC. Most of the iodine remains in the fuel matrix during normal fuel operation. Compounds of cesium and iodine develop in negligible quantities in the gaseous phase at temperatures associated with the fuel-to-sheath gap (~600 K). The major volatile corrosive species, ZrI_4 and I_2, exist in the fuel-to-sheath gap at specific CANDU operating conditions. As burnup increases in the CANDU natural uranium fuel, there is approximately 10 times more cesium. The creation of ^{134}Cs, by activation of ^{133}Cs, causes an additional build-up of cesium fission products. However, these are long-lived species and, to some extent, a second-order effect. The condition set has enough Cs to bind all of the iodine as a $CsI_{(s)}$ salt at equilibrium, but consequently not enough iodine to bind all of the cesium. Thermodynamic arguments agree that the escaping iodine from the UO_2 fuel is made inactive by reacting with the excess cesium fission products to form CsI. However, Cs can form compounds with other elements in the fissioning fuel. Hence, it may be that the I:Cs ratio in the fuel-to-sheath gap is not representative of the overall situation at all stages of burnup and changes in power levels.

The development of Fig. 2a included the chemical species $Zr_{(\alpha)(s)}$, $Zr_{(\beta)(s)}$, $ZrI_{2(s)}$, $ZrI_{3(s)}$, $ZrI_{4(s)}$, $I_{2(s)}$, $I_{(g)}$, $I_{2(g)}$, $ZrI_{4(g)}$, $ZrI_{3(g)}$, $ZrI_{2(g)}$, $ZrI_{(g)}$, and $Zr_{(g)}$. This is a relatively complex system even prior to the introduction of additional elemental components. The volatile iodides ZrI_4, ZrI_3, and ZrI_2 exist at low partial pressures. At high partial pressures, these compounds may crystallize and stifle the transfer of Zr even from a surface not protected by an oxide layer. Fig. 2b demonstrates the effect of a lower pressure, specifically at 10^{-5} atm (1 Pa), i.e., for $Zr_{(s)}$ to coexist in equilibrium with the vapour species at 600 K, the pressure (sum of all Zr–I species) must not exceed 10^{-5} atm (1 Pa). ZrI_4 and pure iodide cause the process of SCC in Zr, where the failure time in ZrI_4 is much shorter than I_2. Elementary iodine reacts with zirconium yielding ZrI_4 and other condensed iodides ZrI_x. In particular, ZrI_4 is the dominant gaseous species in the Zr–I system.

The partial pressure isobars for ZrI_4, in Fig. 3a show an increase with an eventual crest followed by a decrease. As the mole fraction

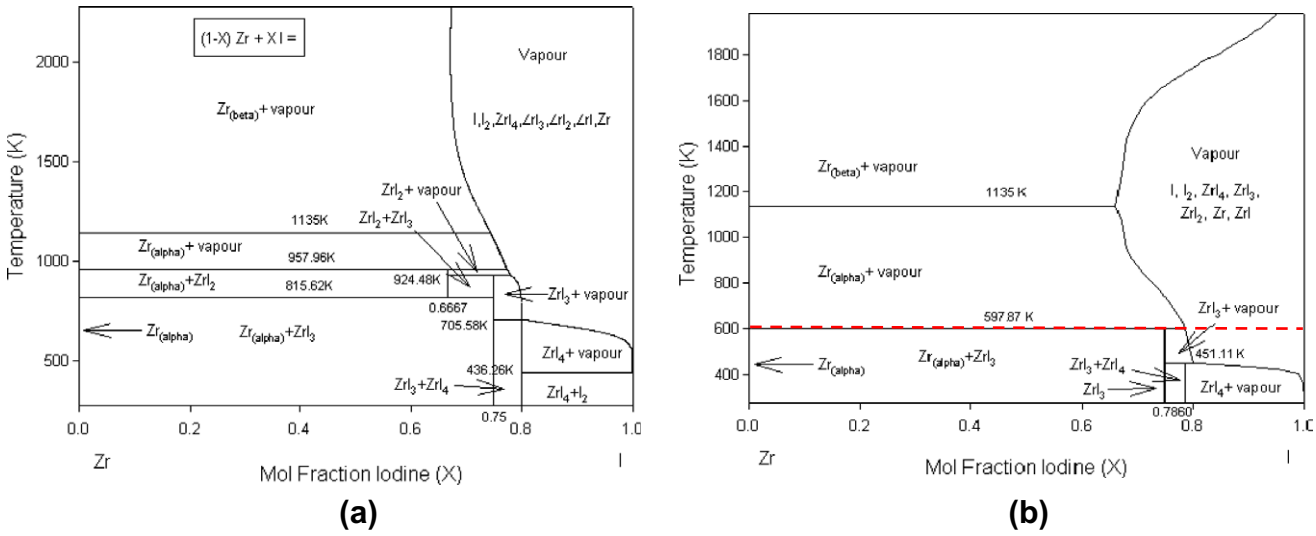

Fig. 2. Calculated phase diagram of the Zr–I system at a hydrostatic (total) pressure of (a) 10^5 Pa (1 atm) and (b) 1 Pa (10^{-5} atm).

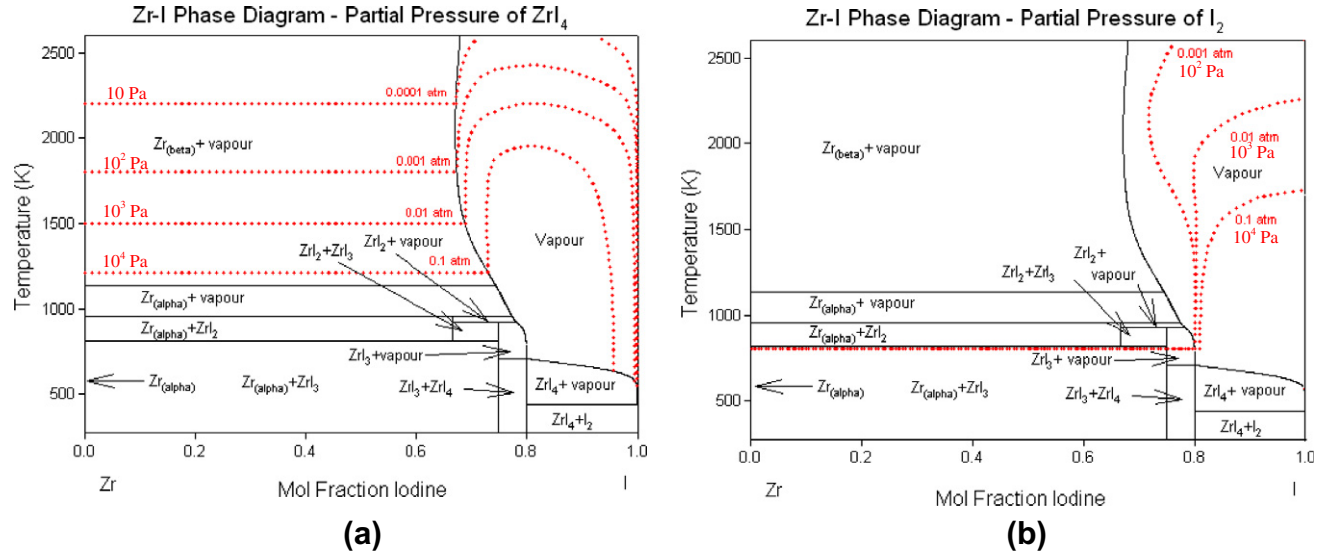

Fig. 3. A calculated phase diagram of the Zr–I system at 10^5 Pa (1 atm) with partial pressure isobars of (a) $ZrI_{4(g)}$ and (b) $I_{2(g)}$.

of I increases, ZrI_4 becomes the more dominant species. However, a saturation limit is reached when more I dilutes ZrI_4, along with the other zirconium iodides, and diatomic iodine becomes more prominent. The maximum is at an approximate overall molar fraction of just above 0.8 for iodine. For example, with the overall molar fraction of 0.82 for iodine at ~755 K, the vapour phase mainly contains: 78% ZrI_4, 22% I_2 with minor quantities of I, ZrI_3 and ZrI_2. On the other hand, for an overall molar fraction for iodine of 0.99 at ~622 K, the vapour phase is composed of 0.7% ZrI_4 and 93.3% I_2 in the vapour phase.

A greater concentration of I_2, in the vapour phase at higher overall molar fractions of I, is depicted by the increasing partial pressure isobars of I_2 in Fig. 3b. In addition, the vertical section of the isobars, between 700–1300 K at a molar fraction just above 0.8 for I, reconfirms ZrI_4 as the dominant species at these conditions, in agreement with Fig. 3a and established literature [19].

2.1. CANLUB chemical analysis

As mentioned in Section 1, thermal expansion of fuel pellets, following an increase in power during re-fuelling, can provide the required strain to initiate a crack in the protective zirconium oxide, ZrO_2, layer on the Zircaloy sheath. Gaseous fission products like iodine released from cracks in the fuel pellet becoming a corrosive agent. To mitigate against SCC, a thin (microns) layer of graphite (mainly carbon) (CANLUB) is applied on the inside layer of the fuel sheath. It is believed that the CANLUB can act as a chemical getter reducing the availability of corrosive fission products that can attack the fuel sheath.

Components of DAG154N used to create the CANLUB by thermal decomposition include isopropanol, graphite, hexylene glycol, *n*-butyl alcohol, and propylene glycol methyl ether. However, the graphite may also contain impurities. Hence, an inductively

coupled plasma mass spectrometry analysis was performed which revealed impurities of silicon, iron, aluminum and sodium that were found in highest quantities [20]. These elements may act as a getter for the iodine or have some other significant role. In particular, iodine will preferentially combine with sodium in the CANLUB.

3. Kinetic model development for crack propagation

The knowledge of the chemistry/thermodynamics, within the fuel-to-sheath gap and crack tip from Section 2 provide the underpinning for a mechanistic kinetics model to explain I-SCC behaviour. An I-SCC kinetics model is developed in this section based on the processes shown in Fig. 4, which accounts for: (i) iodine/cesium diffusional release to the fuel surface by a Booth diffusion process, where the iodine is deposited on the fuel surface as CsI; (ii) a CsI radiolysis model due to fission fragment recoil in order to produce vapour I_2; (iii) transport of I_2 vapour by diffusion along the gap to the crack site; (iii) a reaction of the I_2 at the crack tip to form ZrI_4 vapour which removes the Zr from the crack tip by the Van Arkel process to produce the crack penetration.

3.1. Numerical implementation of the fission-product release model

Diffusion theory is applied to the UO_2 fuel, where an empirical diffusion coefficient accounts for such effects as radiation damage, atomic diffusion, gas-bubble nucleation, bubble migration and bubble coalescence. Hence, a Booth diffusion model is applied to account for the solid-state lattice diffusion of fission products (e.g., iodine) originating from the uranium dioxide (UO_2) fuel matrix, passing through a collection of "equivalent" grain spheres and finally entering the fuel-to-sheath gap [21–23]. The empirical diffusion coefficient can be estimated as a volume-average quantity for the fuel element.

A general time-dependent (numerically based) fission-product diffusion model, coupled with a mass balance in the gap, was developed. The "Booth diffusion" model was generalized for a time-dependent diffusion coefficient $D(t)$ and fission product generation rate at time t (s) [24,25]:

$$\frac{\partial C(r,t)}{\partial t} = \frac{D(t)}{r^2}\frac{\partial}{\partial r}\left(r^2\frac{\partial C(r,t)}{\partial r}\right) - \lambda C(r,t) + \frac{F_f(t)y}{V} \tag{1}$$

Here $C(r, t)$ is the fission product concentration profile at a distance r and time t in an "idealized" fuel grain sphere of radius a. Defining the dimensionless variable $\eta = r/a$ and $u = CV$, and multiplying through by the volume of the fuel in the element, V, Eq. (1) becomes [25]:

$$\frac{\partial u(\eta,t)}{\partial t} = \frac{D'(t)}{\eta^2}\frac{\partial}{\partial \eta}\left(\eta^2\frac{\partial u(\eta,t)}{\partial \eta}\right) - \lambda u(\eta,t) + F_f(t)y \tag{2}$$

where $D'(=D/a^2)$ is the empirical diffusion coefficient (s^{-1}) (see Section 3.3), λ is the decay constant (s^{-1}), F_f is the fission yield for element = $1.489\times10^{13}\,P$ (fission s^{-1}), y is the fission product yield (atom fission^{-1}), and P is the linear element power (kW m^{-1}). The initial and boundary conditions are given as:

$$u(\eta,0) = 0, \quad 0<\eta<1, \quad t=0 \tag{3a}$$

$$\frac{\partial u}{\partial \eta} = 0, \quad \eta = 0, \quad t>0 \tag{3b}$$

$$u(1,t) = 0, \quad \eta = 1, \quad t>0 \tag{3c}$$

The diffusional release-to-birth rate ratio $(R/B)_{diff}$, or release fraction, is defined as the ratio of the total number of atoms released from the sphere compared to the total number of atoms produced within it:

$$\left(\frac{R}{B}\right)_{diff} = \frac{4\pi a^2}{F_f y(4\pi a^3/3)}\left(-D\frac{\partial CV}{\partial r}\bigg|_{r=a}\right) = -\frac{3D'}{F_f y}\frac{\partial u}{\partial \eta}\bigg|_{\eta=1} \tag{4}$$

Equivalently, the diffusive release rate R_{diff} (atom s^{-1}) from the fuel element to the fuel-to-sheath surface (Fick's law) is:

$$R_{diff} = -3D'\frac{\partial u}{\partial \eta}\bigg|_{\eta=1} \tag{5}$$

Note that in the steady-state, Eq. (4) can be analytically solved to give the well-known result for the short-lived species [21]:

$$\left(\frac{R}{B}\right)_{diff} = 3\left[\sqrt{\frac{D'}{\lambda}}\coth\sqrt{\frac{\lambda}{D'}} - \frac{D'}{\lambda}\right] \approx 3\sqrt{\frac{D'}{\lambda}} \tag{6}$$

3.2. Sweep gas analysis

The empirical diffusion coefficient D' in Eq. (2) was derived from fission gas release data for sweep gas experiments conducted at the Chalk River Laboratories (CRL). In particular, a sweep-gas technique investigated the gap inventory within intact operating CANDU-type fuel elements, where the short-lived fission-product release behaviour was measured [24]. During these tests, the fuel-to-sheath gap of an intact element was continually purged with an inert carrier gas flow transporting the active species released from the UO_2 fuel to an out-reactor gamma-ray spectrometer. The instantaneous release rate was measured to determine the physical mechanisms of gas release from the fuel. These experiments covered various irradiation conditions for fuel linear power ratings in the range of 39–65 kW m^{-1} to a maximum fuel burnup of 220 MW h kg^{-1} U^{-1} (see Table 1). Hence, the fission-product release data from these experiments can be used to provide an estimate of the empirical diffusion coefficient for the Booth diffusion model.

The log of the release-to-birth rate ratio (R/B), for the noble gases, was plotted against the log of the decay constant λ for each experiment (see, for example, Fig. 5). This ratio exhibited a behaviour close to $\lambda^{-1/2}$ which, in accordance with Eq. (6), indicating a diffusion-controlled release of fission gas through the UO_2 fuel matrix. However, the fission product iodine was never directly mea-

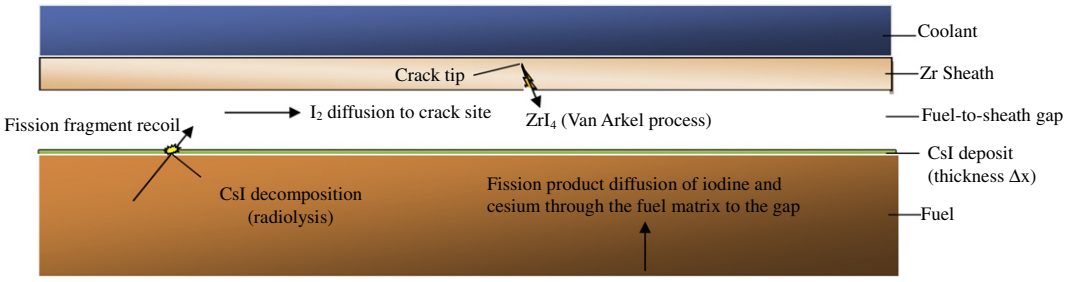

Fig. 4. Schematic of the I-SCC process for crack penetration.

Table 1
Steady-state measured fractional release of various sweep gas experiments[a].

Isotope	Fission yield, y (atoms/fission $\times 10^{-2}$)	Decay constant, λ	R/B for experiment			
			FIO-122	FIO-124	FIO-133	FIO-134
^{133}Xe	6.70	1.52×10^{-6}	7.06×10^{-4}	2.05×10^{-3}	1.42×10^{-3}	5.51×10^{-3}
^{85m}Kr	1.30	4.31×10^{-5}	5.37×10^{-5}	4.08×-10^{-4}	1.35×10^{-4}	9.73×10^{-4}
^{88}Kr	3.55	6.86×10^{-5}	8.82×10^{-5}	1.54×10^{-4}	1.13×10^{-4}	1.30×10^{-3}
^{87}Kr	2.52	1.52×10^{-4}	2.90×10^{-5}	2.90×10^{-4}	1.21×10^{-4}	7.31×10^{-4}
^{135m}Xe	1.10	7.55×10^{-4}	1.80×10^{-5}	3.96×10^{-5}	4.25×10^{-5}	1.60×10^{-4}
^{138}Xe	6.42	8.14×10^{-4}	1.36×10^{-5}	6.36×10^{-5}	5.44×10^{-5}	1.41×10^{-4}
Average linear power (kW/m)			38.2	53.4	50.7	53.6
Average burnup (MW h/kg U)			64.1	40.8	34.9	72.4

[a] Taken from Ref. [43].

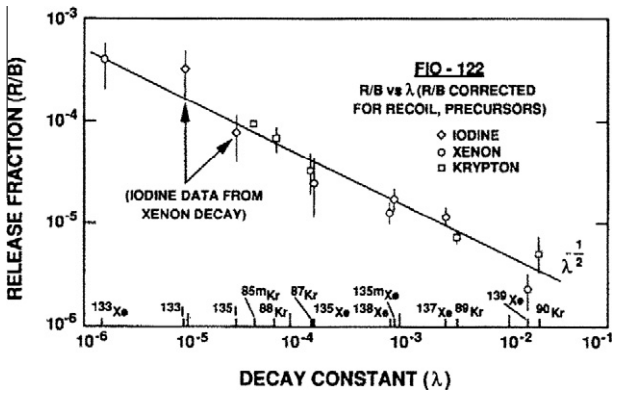

Fig. 5. R/B versus λ for noble gas and iodine isotopes observed or inferred in sweep gas experiment FIO-122.

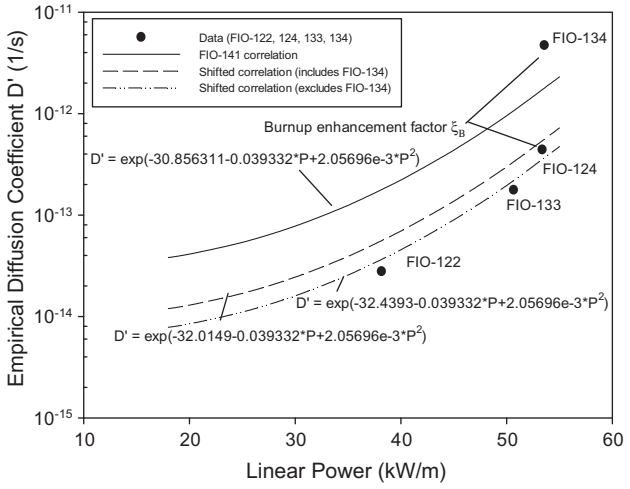

Fig. 6. A fitted empirical diffusion coefficient D' (s^{-1}) of fission gas in the solid fuel matrix calculated as a function of linear fuel element power P (kW m^{-1}) in experiments FIO-122, 124, 133, 134 and 141.

sured by the spectrometer during any phase of normal (intact) operation since this species was absorbed on the internal fuel or sheath surfaces. The iodine release can be deduced from the behaviour of the daughter isotopes, ^{133}Xe and ^{135}Xe, observed with continued sweeping during reactor shutdowns [24]. This analysis indicated a diffusional release behaviour, where the isotopes ^{133}I and ^{135}I also fell on the R/B curves of the noble gases (see Fig. 5). Hence a fitting of Eq. (6) to steady-state (R/B) data from the sweep gas experiments will yield an empirical diffusion coefficient D' (Section 3.2.1).

3.2.1. Diffusion coefficient

The dependence of the solid-state empirical diffusion coefficient, D', as a function of the fuel element linear rating was initially determined from the short-lived ^{138}Xe release data obtained following a stepwise reactor start-up in sweep gas experiment FIO-141 (see Fig. 6) [26]. As depicted in Fig. 6, the fitted empirical diffusion coefficient D' (in s^{-1}) can be given as a function of the fuel element linear power P (in kW m^{-1}) of the form:

$$D'(P) = \exp[a_0 + a_1 P + a_2 P^2] \tag{7}$$

This curve can be suitably scaled to the empirical diffusion coefficients (depicted as solid data points in Fig. 6) for sweep gas experiments FIO-122, 124, 133 and 134. As mentioned, these solid points were derived by fitting of the Booth model in Eq. (6) to the noble gas data in Table 1. The same diffusion coefficient can also be employed for the iodine species based on the results in Fig. 5. Since experiment FIO-134 was conducted with higher burnup fuel, two curves were developed by including and excluding this data point in the fitting. For the current model implementation, the lower curve is chosen for burnup calculations less than 40.8 MW h/kg U, where a "burnup enhancement factor" ζ_B is introduced considering the FIO-134 data point:

$$D' = \exp[-32.0149 - 0.039332P + 2.056960 \times 10^{-3} P^2] * \zeta_B \tag{8}$$

Here ζ_B is given as a simple linear function of the burnup B (in MW h kg U^{-1}):

$$\zeta_B = 0.3065B - 11.5052 \tag{9}$$

This factor is taken as unity for burnups of 40.8 MW h/kg U and smaller.

3.3. Iodine chemistry model

Two requirements for an overall model explaining the I-SCC phenomenon include a required stress to initiate a crack in the protective oxide layer (Section 3.4) and an iodine chemistry model (this section). As shown in Fig. 4, the latter component involves the release of iodine/cesium to the fuel surface (Section 3.3.1), a CsI radiolysis model to produce I_2 vapour for transport in the gap to the crack site (Sections 3.3.2 and 3.3.3), and an instantaneous ZrI_4 reaction at the crack causing crack penetration (Section 3.3.4).

3.3.1. Iodine release to fuel surface

As detailed in Section 3.1, the iodine release to the fuel-to-sheath surface for isotope i can be derived from a "Booth diffusion" model:

$$\frac{\partial u_i}{\partial t} = \frac{D'}{\eta^2}\frac{\partial}{\partial \eta}\left(\eta^2 \frac{\partial u_i}{\partial \eta}\right) - \lambda_i u_i + F_f y_i \tag{10}$$

where the subscript i indicates the seven most important stable (^{127}I and ^{129}I) and radioactive (^{131}I–^{135}I) isotopes of iodine. The diffusive release rate R_{diff} (atom s^{-1}) to the fuel-to-sheath surface (Fick's law) follows from Eq. (5) for each isotope. Based on the sweep gas experimental observations where no iodine was observed in the sweep gas flow (Section 3.2), the deposited concentration $C_{fs,i}$ (atom m^{-2}) of CsI on the fuel surface S_T (m^2) for isotope i is obtained from the mass balance:

$$\frac{dC_{fs,i}}{dt} = \frac{R_{diff,i}}{S_T} - \lambda_i C_{fs,i} \tag{11}$$

Eq. (11) also considers any decay on the deposited fuel surface for the short-lived isotopes. The total deposited concentration on the fuel surface (m^{-2}) is therefore obtained by solving Eq. (11) for each isotope and summing up all contributions:

$$C_{fs,T}(P(t),t) = \sum_{i=I-127,\ldots,135} C_{fs,i}(t) \tag{12}$$

Eq. (12) provides a means to calculate the critical iodine concentration for I-SCC, taking into account iodine produced during the pre-ramp period as well as the rapid production of the short-lived iodine species following the power ramp.

3.3.2. CsI radiolysis model

The CsI radiolysis model requires a release rate of free available iodine R_I (atoms of I s^{-1}) into the gap due to CsI decomposition by fission fragment bombardment (see Section 1). The release rate of a recoil fission fragment from the fuel surface is given by [27–29]:

$$R^{rec} = \frac{1}{4}\mu(S/V)_f F_f y_{ff} \xi_{skin} \tag{13}$$

where μ is the average range of fission fragment in UO_2 (~7.7 μm) (Appendix A), $(S/V)_f$ is the geometric surface-to-volume ratio for the fuel body (~329 m^{-1}), F_f is the fission rate (fission s^{-1}) and y_{ff} is the fission fragment yield (2 recoil particles fission^{-1}). With naturally-enriched fuel, there is a build-up of plutonium (Pu) on the outer edge of the fuel pellet, which enhances the fission rate at this outer layer. An enhancement factor ξ_{skin} can therefore be introduced as detailed in Appendix B.

The release rate of "free" iodine formation from the radiolysis of these recoiling particles is given by:

$$R_I = R^{rec} Y_I (dE/dx) \Delta x \xi_{\text{Canlub}} \xi_{free} \tag{14}$$

Here the particles bombard a thickness Δx (cm) of the deposited CsI. Although the CsI can also recombine after dissociation [30], this effect is ignored as a conservative assumption where no recombination is taken into account. The deposit thickness can be estimated from the solution for $C_{fs,T}$ in Eqs. (11) and (12):

$$\Delta x = \frac{C_{fs,T} M_{\text{CsI}}}{\rho_{\text{CsI}} N_A} \tag{15}$$

where M_{CsI} is the molecular weight of CsI (259.8 g mol^{-1}), ρ_{CsI} is the density of CsI (4.5 g cm^{-3}) and N_A is Avogadro's number (6.022×10^{23} molecule mol^{-1}). The energy loss per path length in the surface deposit (dE/dx) can be evaluated with an SRIM analysis in Appendix A where $dE/dx \sim 460$ eV/Å. As mentioned in Section 1, one iodine atom per 4.35 eV of deposited energy will be liberated so that $Y_I = 0.230$ atom eV^{-1} particle^{-1} [15]. Some of the iodine produced by Eq. (14) will be gettered by the CANLUB interlayer coating. Hence, Eq. (14) contains an additional factor, ξ_{Canlub}, to take into account this effect, where it is considered that the Na impurity will getter the iodine with the formation of the compound NaI, expected to be present as an oxide or carbonate after pyrolysis, i.e., $Na_2O + I_2 \rightarrow 2NaI + ½O_2$ and $Na_2CO_3 + I_2 \rightarrow 2NaI + ½O_2 + CO_2$.

$$\xi_{\text{Canlub}} = \frac{C_{fs,T} - C_{\text{Na}}}{C_{fs,T}} \tag{16}$$

Here the sodium surface concentration (atom m^{-2}) is evaluated from:

$$C_{\text{Na}} = \frac{w_{\text{Na}} \rho_{\text{Canlub}} \Delta t_{\text{Canlub}} N_A}{A_{\text{Na}}} \tag{17}$$

where w_{Na} is the impurity content by weight of sodium in the CANLUB (=137 × 10^{-6} g of Na/g of CANLUB) [20], ρ_{Canlub} is the CANLUB density (~0.9 g cm^{-3}), Δt_{Canlub} (m) is the coating thickness (i.e., the typical thickness is ~5 μm for thick CANLUB, with thin layers around 2.5 μm), N_A is Avogadro's number (6.022×10^{23} atom mol^{-1}), and A_{Canlub} is the atomic weight of sodium (22.98977 g mol^{-1}). As a simplifying assumption, the radiolysis of NaI is not considered in this analysis.

Finally, a critical tensile stress in the sheath is needed to relax the compressive stress and then crack the protective oxide layer in order to initiate crack formation in the sheath metal, as well as to maintain a sufficient stress at the crack tip [31] so that SCC can continue (Section 1). Thus, ξ_{free} in Eq. (14) equals unity when the appropriate stress/strain conditions are met as detailed in Section 3.4. Otherwise it is set equal to zero so that no iodine can react at the crack tip. The production rate of "free" molecular iodine (I_2) (molecules of I_2 s^{-1}) is

$$R_{I_2} = \frac{1}{2} R_I \tag{18}$$

Hence, Eq. (18) provides the source of "free" molecular iodine that is available to diffuse in the gap as a vapour to the crack site (see Section 3.3.3), when the protective oxide has been breached at the time of crack formation (i.e., t_{dwell}).

3.3.3. I_2 gap transport model

The volatile I_2 can diffuse to a site where the protective oxide is cracked to promote crack propagation. The I_2 transport model requires a source term for the release rate (per path length ℓ_f for the fuel stack) of $I_{2(g)}$ for a given isotope i ($R_{g,i}$) in the fuel-to-sheath gap (molecules of I_2 m^{-1} s^{-1}):

$$R_{g,i} = \frac{R_{I_2}}{\ell_f}\left(\frac{C_{fs,i}}{C_{fs,T}}\right) \tag{19}$$

where R_{I_2} is given by Eq. (18). The concentration profile in the fuel-to-sheath gap for isotope i, $C_{g,i}$ (molecule m^{-1}), follows from the transport equation for molecular gas-phase diffusion (see Fig. 8):

Table 2
Representative cases for threshold-failure probability model.

Case	Fuel properties		Irradiation conditions				Failure	
Identification	CANLUB	Sheath inner diameter (mm)	Burnup (MW h/kg U)	Initial power (kW/m)	Ramped power (kW/m)	Dwell time (h)	Observed	Predicted (h)
PS/1988/OE	Thick	14.409	188.7	32.4	52.5	0.7	NO	NO
EXP-1/HP/OE	Thin	12.240	80.0	31.0	57.5	>2.5	YES	1.5
EXP-2(356)	No CANLUB	14.409	240.0	22.9	36.4	>2.5	YES	0.5

Table 3
Comparison of model predictions against validation database of power ramp experience.

Case	Fuel properties		Irradiation conditions				Failure		Case	Fuel Properties		Irradiation Conditions				Failure	
Identification	CANLUB	Sheath inner diameter (mm)	Burnup (MW h/kg U)	Initial power (kW/m)	Ramped power (kW/m)	Dwell time (h)	Observed	Predicted (h)	Identification	CANLUB	Sheath inner diameter (mm)	Burnup (MW h/kg U)	Initial power (kW/m)	Ramped power (kW/m)	Dwell time (h)	Observed	Predicted (h)
PS/1988/OE	Thick	14.409	45.5	35.6	58.4	0.7	NO	NO	EXP-4 PA98	Thick	14.340	95.0	41.0	55.0	>2.5	NO	NO
PS/1988/OE	Thick	14.409	50.0	37.3	58.5	0.7	NO	NO	EXP-3/4700/01	Thick	14.340	100.0	42.1	71.3	>2.5	NO	0.4
PS/1988/OE	Thick	14.409	53.3	39.2	58.4	0.7	NO	NO	EXP-3/4900/11	Thick	14.340	104.0	44.0	64.0	>2.5	NO	NO
PS/1988/OE	Thick	14.409	56.6	38.1	58.4	0.7	NO	NO	EXP-4/3400/01,04	Thick	14.310	131.0	35.0	64.0	>2.5	NO	0.7
PS/1988/OE	Thick	14.409	67.7	38.1	63.3	0.7	NO	NO	EXP-4/3400/03,06	Thick	14.300	124.0	35.0	64.0	>2.5	NO	0.4
PS/1988/OE	Thick	14.409	72.2	36.4	61.2	0.7	NO	NO	EXP-5/IE PA62	Thick	14.290	313.0	34.0	43.0	>2.5	NO	NO
PS/1988/OE	Thick	14.409	77.7	38.0	63.4	0.7	NO	NO	EXP-3/4800/03	Thick	14.220	121.0	41.0	65.0	>2.5	YES	NO
PS/1988/OE	Thick	14.409	78.8	39.7	61.6	0.7	YES	NO	EXP-3/4800/01	Thick	14.220	259.0	60.5	72.0	>2.5	NO	NO
PS/1988/OE	Thick	14.409	81.0	36.7	58.8	0.7	NO	NO	EXP-3/4600/01	Thick	14.160	100	39	66	>2.5	YES	NO
PS/1988/OE	Thick	14.409	81.0	38.8	62.9	0.7	NO	NO	EXP-5/OE PA16	Thick	13.736	448.0	49.0	68.7	>2.5	NO	0.3
PS/1988/OE	Thick	14.409	88.8	36.1	60.6	0.7	YES	NO	EXP-5/02 (16)	Thick	13.736	448.0	49.0	68.7	>2.5	NO	0.3
PS/1988/OE	Thick	14.409	89.9	36.0	60.1	0.7	NO	NO	EXP-5/IE PA1	Thick	13.735	360.0	28.0	40.0	>2.5	NO	NO
PS/1988/OE	Thick	14.409	92.1	35.6	56.2	0.7	NO	NO	EXP-5/IE PA1	Thick	13.735	365.0	28.0	54.0	>2.5	NO	0.6
PS/1988/OE	Thick	14.409	92.1	36.0	55.8	0.7	NO	NO	EXP-5/IE PA15	Thick	13.735	392.0	28.0	40.0	>2.5	NO	NO
PS/1988/OE	Thick	14.409	96.6	38.5	62.3	0.7	NO	NO	EXP-5/OE PA1	Thick	13.735	465.0	40.0	52.0	>2.5	NO	NO
PS/1988/OE	Thick	14.409	97.7	39.1	60.3	0.7	NO	NO	EXP-6 (34)	Thick	13.716	480.0	35.0	47.0	>2.5	NO	NO
PS/1988/OE	Thick	14.409	101.0	37.1	57.5	0.7	NO	NO	EXP-6 (36)	Thick	13.716	495.0	31.3	51.0	>2.5	NO	0.3
PS/1988/OE	Thick	14.409	102.1	38.3	55.9	0.7	NO	NO	EXP-5/PA32	Thick	12.914	142.0	36.0	61.0	>2.5	NO	0.4
PS/1988/OE	Thick	14.409	112.1	35.4	60.2	0.7	NO	NO	EXP-3/AH17	Thick	12.444	72.4	27.7	59.3	>2.5	NO	NO
PS/1988/OE	Thick	14.409	119.9	35.2	58.1	0.7	NO	NO	EXP-3/8500/21	Thick	12.251	106.0	43.9	59.5	>2.5	NO	NO
PS/1988/OE	Thick	14.409	122.1	35.6	49.8	0.7	NO	NO	EXP-3/8500/01	Thick	12.251	114.0	30.7	64.5	>2.5	NO	0.4
PS/1988/OE	Thick	14.409	123.2	35.7	58.6	0.7	NO	NO	EXP-5(12)	Thick	12.251	124.0	5.2	20.1	>2.5	NO	NO
PS/1988/OE	Thick	14.409	123.2	37.7	57.4	0.7	NO	NO	EXP-5 (07)	Thick	12.251	155.0	9.8	30.3	>2.5	NO	NO
PS/1988/OE	Thick	14.409	124.3	35.2	59.2	0.7	NO	NO	EXP-5 (11)	Thick	12.251	157.0	4.6	17.6	>2.5	NO	NO
PS/1988/OE	Thick	14.409	126.5	36.9	56.4	0.7	NO	NO	EXP-3/8500/11	Thick	12.251	180.0	27.3	57.8	>2.5	NO	0.8
PS/1988/OE	Thick	14.409	126.5	37.1	49.4	0.7	NO	NO	EXP-5 (10)	Thick	12.251	223.0	8.3	31.6	>2.5	NO	NO
PS/1988/OE	Thick	14.409	127.7	36.7	55.4	0.7	NO	NO	EXP-5 (09)	Thick	12.251	270.0	7.7	29.4	>2.5	NO	NO
PS/1988/OE	Thick	14.409	127.7	37.1	58.2	0.7	NO	NO	EXP-5/ PA9	Thick	12.242	170.0	30.0	36.0	>2.5	NO	NO
PS/1988/OE	Thick	14.409	127.7	38.1	57.5	0.7	NO	NO	PS-2/J64728C/OE	Thick	12.239	196.7	11.5	44.6	>2.5	YES	NO
PS/1988/OE	Thick	14.409	128.8	35.0	49.0	0.7	NO	NO	EXP-5/18	Thick	12.233	80.8	30.7	64.0	>2.5	YES	0.7
PS/1988/OE	Thick	14.409	128.8	36.4	56.7	0.7	NO	NO	EXP-5/07	Thick	12.230	80.8	30.7	64.0	>2.5	YES	0.7
PS/1988/OE	Thick	14.409	128.8	45.1	53.2	0.7	NO	NO	EXP-5/INTER	Thick	12.225	100.0	26.0	52.0	>2.5	NO	NO
PS/1988/OE	Thick	14.409	129.9	35.1	59.3	0.7	YES	0.6	EXP-5/IE PA1	Thick	12.223	79.0	21.0	50.0	>2.5	NO	NO

(*continued on next page*)

Table 3 (*continued*)

Case	Fuel properties		Irradiation conditions				Failure		Case	Fuel Properties		Irradiation Conditions				Failure	
Identification	CANLUB	Sheath inner diameter (mm)	Burnup (MW h/kg U)	Initial power (kW/m)	Ramped power (kW/m)	Dwell time (h)	Observed	Predicted (h)	Identification	CANLUB	Sheath inner diameter (mm)	Burnup (MW h/kg U)	Initial power (kW/m)	Ramped power (kW/m)	Dwell time (h)	Observed	Predicted (h)
PS/1988/OE	Thick	14.409	129.9	36.5	56.9	0.7	NO	NO	EXP-5/IE PA2	Thick	12.223	87.0	21.0	51.0	>2.5	NO	1.4
PS/1988/OE	Thick	14.409	129.9	37.0	58.9	0.7	NO	NO	EXP-5/OE PA	Thick	12.223	96.0	22.6	53.1	>2.5	NO	1.2
PS/1988/OE	Thick	14.409	129.9	37.5	59.3	0.7	YES	NO	EXP-5/INTE	Thick	12.223	96.0	26.0	60.0	>2.5	YES	0.5
PS/1988/OE	Thick	14.409	131.0	37.3	60.8	0.7	YES	NO	EXP-5/OE PA	Thick	12.223	106.0	23.5	53.9	>2.5	NO	0.6
PS/1988/OE	Thick	14.409	133.2	34.9	58.7	0.7	YES	0.4	EXP-5/INTE	Thick	12.223	106.0	27.0	61.0	>2.5	YES	2.0
PS/1988/OE	Thick	14.409	133.2	35.1	58.9	0.7	NO	0.5	EXP-5/22 PA2	Thick	12.222	52.1	20.4	42.6	>2.5	NO	NO
PS/1988/OE	Thick	14.409	133.2	39.1	57.9	0.7	NO	NO	EXP-5/IE PA3	Thick	12.222	88.0	23.0	46.0	>2.5	NO	NO
PS/1988/OE	Thick	14.409	133.2	46.4	53.4	0.7	NO	NO	EXP-5/PA27	Thick	12.222	101.0	33.0	43.0	>2.5	NO	NO
PS/1988/OE	Thick	14.409	135.4	37.3	56.0	0.7	NO	NO	EXP-5/22 PA2	Thick	12.222	104.0	42.5	51.2	>2.5	NO	NO
PS/1988/OE	Thick	14.409	135.4	39.1	56.7	0.7	YES	NO	EXP-5 PA38	Thick	12.221	58.0	20.0	43.0	>2.5	NO	NO
PS/1988/OE	Thick	14.409	139.9	35.6	44.1	0.7	NO	NO	EXP-5 PA39	Thick	12.221	94.0	35.0	71.0	>2.5	NO	0.4
PS/1988/OE	Thick	14.409	143.2	37.8	44.2	0.7	NO	NO	EXP-3/9700 PA94	Thick	12.221	112.0	37.0	63.0	>2.5	NO	0.4
PS/1988/OE	Thick	14.409	144.3	37.0	41.9	0.7	NO	NO	EXP-3/9700/OE2	Thick	12.221	125.0	34.0	64.0	>2.5	NO	0.4
PS/1988/OE	Thick	14.409	147.6	34.5	55.1	0.7	YES	NO	EXP-3/9700/OE3	Thick	12.221	125.0	34.0	64.0	>2.5	NO	0.4
PS/1988/OE	Thick	14.409	152.1	33.3	44.9	0.7	NO	NO	EXP-3/9700/OE4	Thick	12.221	125.0	34.0	64.0	>2.5	NO	0.4
PS/1988/OE	Thick	14.409	152.1	35.1	44.9	0.7	NO	NO	EXP-3/7800/06	Thick	12.221	132.0	36.0	58.0	>2.5	YES	NO
PS/1988/OE	Thick	14.409	153.2	36.7	44.4	0.7	NO	NO	EXP-5/ PA10	Thick	12.221	218.0	39.0	48.0	>2.5	NO	NO
PS/1988/OE	Thick	14.409	163.2	33.1	54.3	0.7	NO	NO	EXP-3/7800/12	Thick	12.221	338.0	28.2	61.0	>2.5	YES	0.3
PS/1988/OE	Thick	14.409	164.3	43.5	50.0	0.7	NO	NO	PS-2/OE-1	Thick	12.22	127.1	49.0	59.7	>2.5	YES	NO
PS/1988/OE	Thick	14.409	165.4	33.8	53.4	0.7	YES	NO	PS-2/OE-2	Thick	12.22	128.1	49.2	59.9	>2.5	YES	NO
PS/1988/OE	Thick	14.409	166.5	34.2	53.1	0.7	NO	NO	EXP-5/PA29	Thick	12.215	142.0	36.0	61.0	>2.5	NO	0.4
PS/1988/OE	Thick	14.409	166.5	35.1	51.3	0.7	NO	NO	EXP-5/06 PA3	Thick	12.215	155.0	57.1	70.2	>2.5	NO	NO
PS/1988/OE	Thick	14.409	167.6	33.4	52.4	0.7	NO	NO	EXP-5/11 PA3	Thick	12.215	155.0	57.1	70.2	>2.5	NO	NO
PS/1988/OE	Thick	14.409	167.6	34.4	52.3	0.7	NO	NO	EXP-3/8700/01	Thick	12.213	129.0	30.1	61.1	>2.5	YES	0.4
PS/1988/OE	Thick	14.409	172.1	33.5	52.7	0.7	NO	NO	EXP-3/8000/01	Thick	12.207	114.0	30.4	63.9	>2.5	NO	0.4
PS/1988/OE	Thick	14.409	173.2	33.3	53.2	0.7	NO	NO	EXP-3/8000/23	Thick	12.206	114.0	30.4	63.9	>2.5	NO	0.4
PS/1988/OE	Thick	14.409	174.3	34.9	54.4	0.7	NO	NO	EXP-5/IE PA3	Thick	12.201	127.0	33.0	66.0	>2.5	NO	0.5
PS/1988/OE	Thick	14.409	175.4	34.1	52.2	0.7	NO	NO	EXP-3/8000/29	Thick	12.199	180.0	27.0	57.2	>2.5	YES	0.4
PS/1988/OE	Thick	14.409	175.4	36.1	51.6	0.7	NO	NO	EXP-3/8000/35	Thick	12.194	132.0	31.3	57.3	>2.5	NO	0.4
PS/1988/OE	Thick	14.409	176.5	34.9	52.0	0.7	YES	NO	EXP-5/O3 PA8	Thick	12.191	81.0	32.0	62.0	>2.5	NO	NO
PS/1988/OE	Thick	14.409	176.5	35.3	51.5	0.7	NO	NO	EXP-5/02 PA7	Thick	12.184	81.0	32.0	45.0	>2.5	NO	NO
PS/1988/OE	Thick	14.409	179.8	35.1	51.6	0.7	NO	NO	EXP-3/7200/14	Thick	12.170	91.0	37.0	61.0	>2.5	YES	NO

PS/1988/OE	Thick	14.409	180.9	34.9	53.7	0.7	YES	NO	EXP-3/7200/31	Thick	12.170	103.0	40.0	62.0	>2.5	NO	NO
PS/1988/OE	Thick	14.409	182.0	32.3	43.7	0.7	NO	NO	EXP-7/MIDDLE	Thick	10.777	176.0	28.6	45.4	>2.5	NO	NO
PS/1988/OE	Thick	14.409	182.0	32.5	51.3	0.7	NO	NO	FFO-104	Thick	12.15	240	30	58	0.3	YES	0.3
PS/1988/OE	Thick	14.409	182.0	34.5	51.7	0.7	NO	NO	EXP-1/Inter	Thin	12.240	63.0	27.0	44.0	>2.5	NO	NO
PS/1988/OE	Thick	14.409	182.0	34.6	51.2	0.7	NO	NO	EXP-3/4300/10	Thin	14.389	100.0	37.0	61.0	>2.5	YES	0.6
PS/1988/OE	Thick	14.409	183.2	32.7	53.3	0.7	YES	NO	EXP-5 PA43	Thin	14.350	82.0	17.0	64.0	>2.5	YES	0.9
PS/1988/OE	Thick	14.409	183.2	35.2	50.3	0.7	NO	NO	EXP-5 PA45	Thin	14.350	92.0	18.0	58.0	>2.5	YES	1.2
PS/1988/OE	Thick	14.409	184.3	32.7	53.2	0.7	NO	NO	EXP-5/3	Thin	14.350	95.0	11.0	37.2	>2.5	NO	1.2
PS/1988/OE	Thick	14.409	184.3	33.0	52.1	0.7	NO	NO	EXP-5/6	Thin	14.350	95.0	13.1	44.4	>2.5	NO	0.6
PS/1988/OE	Thick	14.409	184.3	35.4	50.7	0.7	NO	NO	EXP-5/3	Thin	14.350	148.0	29.2	46.7	>2.5	NO	NO
PS/1988/OE	Thick	14.409	184.3	36.5	50.4	0.7	NO	NO	EXP-5/6	Thin	14.350	148.0	34.8	55.7	>2.5	NO	0.4
PS/1988/OE	Thick	14.409	186.5	34.8	50.5	0.7	YES	NO	EXP-5/OE	Thin	14.350	167.0	50.0	60.0	>2.5	NO	NO
PS/1988/OE	Thick	14.409	187.6	33.2	52.4	0.7	NO	NO	EXP-5/1	Thin	14.350	192.0	29.9	36.5	>2.5	NO	NO
PS/1988/OE	Thick	14.409	188.7	33.2	51.1	0.7	NO	NO	EXP-5/7	Thin	14.350	192.0	35.7	43.5	>2.5	NO	NO
PS/1988/OE	Thick	14.409	190.9	36.7	50.6	0.7	NO	NO	EXP-5–42	Thin	14.350	214.0	39.0	52.0	>2.5	YES	NO
PS/1988/OE	Thick	14.409	192.0	33.7	43.4	0.7	NO	NO	EXP-3/08	Thin	12.251	86.4	30.7	70.3	>2.5	NO	0.5
PS/1988/OE	Thick	14.409	192.0	34.1	51.5	0.7	NO	NO	EXP-3/15	Thin	12.251	86.4	30.7	70.3	>2.5	NO	0.5
PS/1988/OE	Thick	14.409	192.0	40.3	47.6	0.7	NO	NO	EXP-3/01	Thin	12.251	86.4	30.7	70.3	>2.5	YES	0.5
PS/1988/OE	Thick	14.409	193.1	34.6	49.4	0.7	NO	NO	EXP-1/INTER	Thin	12.240	133.0	38.0	45.0	>2.5	NO	NO
PS/1988/OE	Thick	14.409	194.3	31.5	42.8	0.7	NO	NO	EXP-1/OE	Thin	12.223	172.0	45.0	56.0	>2.5	YES	NO
PS/1988/OE	Thick	14.409	194.3	34.7	52.1	0.7	NO	NO	EXP-3/9700/OE1	Thin	12.221	125.0	34.0	64.0	>2.5	YES	0.4
PS/1988/OE	Thick	14.409	196.5	31.7	43.1	0.7	NO	NO	EXP-1/Inter	Thin	12.214	140.0	38.0	45.0	>2.5	NO	NO
PS/1988/OE	Thick	14.409	196.5	33.0	55.8	0.7	YES	0.3	EXP-1/OE	Thin	12.205	179.0	47.0	58.0	>2.5	NO	NO
PS/1988/OE	Thick	14.409	196.5	33.6	43.0	0.7	NO	NO	PS/1972/OE	NO	14.409	46	9.8	45.8	0.3	NO	NO
PS/1988/OE	Thick	14.409	196.5	36.1	50.9	0.7	NO	NO	EXP-4(16)	NO	14.409	46.0	45.9	73.6	>2.5	YES	NO
PS/1988/OE	Thick	14.409	197.6	34.4	53.2	0.7	YES	NO	PS/1972/OE	NO	14.409	50	9.8	54.3	0.3	YES	2.2
PS/1988/OE	Thick	14.409	198.7	31.8	42.9	0.7	NO	NO	EXP-2(137)	NO	14.409	50.0	28.6	49.4	>2.5	NO	NO
PS/1988/OE	Thick	14.409	198.7	33.5	55.6	0.7	YES	0.4	PS/1972/OE	NO	14.409	51	12.6	43.5	0.3	NO	NO
PS/1988/OE	Thick	14.409	198.7	34.0	50.4	0.7	NO	NO	PS/1972/OE	NO	14.409	52	8.8	46.3	0.3	NO	3.0
PS/1988/OE	Thick	14.409	199.8	34.2	50.9	0.7	NO	NO	PS/1972/OE	NO	14.409	54	13.6	48.4	0.3	NO	2.5
PS/1988/OE	Thick	14.409	199.8	42.1	48.5	0.7	NO	NO	PS/1972/OE	NO	14.409	56	13.6	42.8	0.3	NO	NO
PS/1988/OE	Thick	14.409	200.9	33.3	55.0	0.7	YES	0.4	PS/1972/OE	NO	14.409	58	12.9	53.2	0.3	YES	1.9
PS/1988/OE	Thick	14.409	200.9	35.1	50.2	0.7	NO	NO	EXP-2(117)	NO	14.409	82.0	26.2	44.7	>2.5	NO	NO
PS/1988/OE	Thick	14.409	200.9	42.2	47.6	0.7	NO	NO	EXP-2(75)	NO	14.409	83.0	27.1	42.7	>2.5	NO	NO
PS/1988/OE	Thick	14.409	202.0	34.5	49.0	0.7	NO	NO	EXP-2(103)	NO	14.409	85.0	27.4	43.9	>2.5	NO	NO
PS/1988/OE	Thick	14.409	203.1	34.1	53.6	0.7	YES	NO	EXP-2(170)	NO	14.409	89.0	23.5	46.1	>2.5	NO	NO
PS/1988/OE	Thick	14.409	203.1	35.0	55.0	0.7	YES	NO	PS/1972/OE	NO	14.409	97	25.8	45.8	0.3	NO	NO
PS/1988/OE	Thick	14.409	203.1	43.6	47.1	0.7	NO	NO	EXP-2(375)	NO	14.409	102.0	25.3	53.5	>2.5	YES	2.5
PS/1988/OE	Thick	14.409	204.2	34.2	56.8	0.7	YES	0.4	EXP-6/OE	NO	14.33	104.0	24.2	51.7	>2.5	YES	1.4
PS/1988/OE	Thick	14.409	205.4	33.2	48.5	0.7	NO	NO	PS/1972/OE	NO	14.409	107	22.1	43.3	0.3	NO	1.1
PS/1988/OE	Thick	14.409	205.4	33.9	48.5	0.7	NO	NO	EXP-4(06)	NO	14.409	107.0	37.7	56.5	>2.5	YES	NO
PS/1988/OE	Thick	14.409	206.5	35.6	53.7	0.7	YES	NO	EXP-4(05)	NO	14.409	109.0	27.6	57.8	>2.5	YES	0.8
PS/1988/OE	Thick	14.409	206.5	36.3	54.2	0.7	YES	NO	EXP-2(07)	NO	14.409	112.0	33.9	38.1	>2.5	NO	NO
PS/1988/OE	Thick	14.409	207.6	32.7	55.0	0.7	YES	0.4	PS/1972/OE	NO	14.409	119	24.8	41.6	0.3	NO	NO
PS/1988/OE	Thick	14.409	208.7	34.2	54.7	0.7	YES	0.4	PS/1972/OE	NO	14.409	124	23.8	42.1	0.3	NO	NO
PS/1988/OE	Thick	14.409	210.9	35.0	57.0	0.7	YES	0.4	PS/1972/OE	NO	14.409	126	27.0	47.5	0.3	YES	1.3
PS/1988/OE	Thick	14.409	210.9	35.7	53.9	0.7	YES	NO	PS/1972/OE	NO	14.409	128	25.6	47.6	0.3	YES	0.8
PS/1988/OE	Thick	14.409	210.9	41.4	49.3	0.7	NO	NO	PS/1972/OE	NO	14.409	129	24.8	49.1	0.3	YES	0.8
PS/1988/OE	Thick	14.409	214.2	34.8	55.1	0.7	YES	0.3	PS/1972/OE	NO	14.409	131	24.5	54	0.3	YES	0.4
PS/1988/OE	Thick	14.409	215.3	43.4	50.4	0.7	NO	NO	PS/1972/OE	NO	14.409	132	26.9	48.7	0.3	YES	0.5
PS/1988/OE	Thick	14.409	217.6	33.0	53.8	0.7	YES	0.3	PS/1972/OE	NO	14.409	133	23.5	47.2	0.3	YES	1.3
PS/1988/OE	Thick	14.409	218.7	34.3	45.7	0.7	NO	NO	PS/1972/OE	NO	14.409	134	25.8	48.4	0.3	YES	0.4
PS/1988/OE	Thick	14.409	218.7	36.4	52.8	0.7	YES	NO	PS/1972/OE	NO	14.409	134	27.9	46.9	0.3	YES	1.3
PS/1988/OE	Thick	14.409	219.8	32.6	54.4	0.7	YES	0.4	PS/1972/OE	NO	14.409	135	26.5	58.3	0.3	YES	0.5

(*continued on next page*)

Table 3 (*continued*)

Case	Fuel properties		Irradiation conditions				Failure		Case	Fuel Properties		Irradiation Conditions				Failure	
Identification	CANLUB	Sheath inner diameter (mm)	Burnup (MW h/kg U)	Initial power (kW/m)	Ramped power (kW/m)	Dwell time (h)	Observed	Predicted (h)	Identification	CANLUB	Sheath inner diameter (mm)	Burnup (MW h/kg U)	Initial power (kW/m)	Ramped power (kW/m)	Dwell time (h)	Observed	Predicted (h)
PS/1988/OE	Thick	14.409	220.9	32.7	55.2	0.7	YES	0.4	PS/1972/OE	NO	14.409	136	27.9	51.5	0.3	YES	0.7
PS/1988/OE	Thick	14.409	223.1	33.8	52.3	0.7	YES	NO	PS/1972/OE	NO	14.409	137	24.6	47.6	0.3	YES	1.3
PS/1988/OE	Thick	14.409	224.2	32.5	45.8	0.7	NO	NO	PS/1972/OE	NO	14.409	137	27.1	52.8	0.3	YES	0.6
PS/1988/OE	Thick	14.409	224.2	32.6	45.7	0.7	NO	NO	PS/1972/OE	NO	14.409	137	29.1	50.5	0.3	YES	0.4
PS/1988/OE	Thick	14.409	225.3	45.2	49.3	0.7	NO	NO	PS/1972/OE	NO	14.409	138	26.3	52.2	0.3	YES	0.6
PS/1988/OE	Thick	14.409	226.4	40.7	46.4	0.7	NO	NO	PS/1972/OE	NO	14.409	144	25.6	49.3	0.3	YES	0.5
PS/1988/OE	Thick	14.409	227.6	32.7	51.3	0.7	YES	NO	PS/1972/OE	NO	14.409	145	27.7	56.1	0.3	YES	0.4
PS/1988/OE	Thick	14.409	227.6	33.7	55.6	0.7	YES	0.4	EXP-2(366)	NO	14.409	150.0	28.8	45.9	>2.5	YES	NO
PS/1988/OE	Thick	14.409	228.7	32.9	41.8	0.7	NO	NO	EXP-2(369)	NO	14.409	150.0	34.8	44.6	>2.5	YES	NO
PS/1988/OE	Thick	14.409	230.9	34.5	51.7	0.7	YES	NO	PS-3(08)	NO	14.409	150.0	52.6	55.4	>2.5	YES	NO
PS/1988/OE	Thick	14.409	242.0	42.2	48.5	0.7	NO	NO	EXP-2(368)	NO	14.409	151.0	34.1	44.3	>2.5	YES	NO
PS/1988/OE	Thick	14.409	243.1	41.8	48.5	0.7	NO	NO	PS-3(07)	NO	14.409	151.0	49.8	52.9	>2.5	YES	NO
PS/1988/OE	Thick	14.409	252.0	39.8	45.3	0.7	NO	NO	PS/1972/OE	NO	14.409	152	29.3	55.2	0.3	YES	0.4
EXP-4/3000/03,07	Thick	14.417	68.0	25.0	60.0	>2.5	NO	1.6	EXP-4/97	Thick	14.340	93.0	51.0	64.0	>2.5	NO	NO
EXP-4/3000/23	Thick	14.404	54.0	19.0	60.0	>2.5	NO	1.9	EXP-2(387)	NO	14.409	154.0	41.7	43.6	>2.5	YES	NO
EXP-4/3000/19	Thick	14.404	55.0	19.0	60.0	>2.5	NO	2.0	EXP-2(269)	NO	14.409	159.0	25.2	35.8	>2.5	NO	NO
EXP-3/7700/15	Thick	14.404	550.0	34.4	60.1	>2.5	NO	0.3	EXP-2(364)	NO	14.409	170.0	28.9	41.7	>2.5	YES	NO
EXP-4/3000/22	Thick	14.403	108.0	40.0	56.0	>2.5	NO	NO	EXP-2(365)	NO	14.409	172.0	27.4	44.3	>2.5	YES	0.4
EXP-8 PA114	Thick	14.395	69.0	40.0	87.0	>2.5	NO	0.3	EXP-2(243)	NO	14.409	178.0	27.1	38.3	>2.5	NO	NO
EXP-8/PA116	Thick	14.395	69.0	40.0	87.0	>2.5	NO	0.3	EXP-4(04)	NO	14.409	179.0	42.3	62.6	>2.5	YES	0.4
EXP-8 PA115	Thick	14.395	177.0	59.0	87.0	>2.5	NO	0.3	EXP-2(386)	NO	14.409	180.0	40.7	45.3	>2.5	YES	NO
EXP-3 166 PA74	Thick	14.389	107.0	35.0	70.0	>2.5	YES	0.4	EXP-2(230)	NO	14.409	185.0	20.2	31.1	>2.5	NO	NO
EXP-6 (35)	Thick	14.380	472.0	51.8	69.5	>2.5	NO	0.3	PS-3(06)	NO	14.409	186.0	46.6	50.9	>2.5	YES	NO
EXP-5/OE PA1	Thick	14.379	99.0	34.8	68.7	>2.5	NO	0.6	EXP-2(363)	NO	14.409	189.0	26.2	41.6	>2.5	YES	0.4
EXP-3/5100/07	Thick	14.370	121.0	40.7	64.7	>2.5	YES	NO	EXP-2(385)	NO	14.409	190.0	38.8	42.5	>2.5	YES	NO
EXP-3/5200/07	Thick	14.370	121.0	40.9	65.0	>2.5	YES	NO	EXP-2(282)	NO	14.409	196.0	21.9	31.2	>2.5	NO	NO
EXP-5 PA1	Thick	14.369	51.0	20.9	40.9	>2.5	NO	NO	EXP-4(03)	NO	14.409	196.0	42.4	61.7	>2.5	YES	0.5
EXP-3/5000/05	Thick	14.360	104.0	42.0	66.0	>2.5	YES	NO	EXP-2(362)	NO	14.409	199.0	25.0	40.6	>2.5	YES	0.4
EXP-3/5000/20	Thick	14.360	121.0	41.0	65.0	>2.5	YES	NO	EXP-2(361)	NO	14.409	200.0	23.1	35.1	>2.5	YES	NO
EXP-5 PA54	Thick	14.350	49.0	11.0	42.0	>2.5	NO	NO	PS-3(05)	NO	14.409	200.0	42.5	45.3	>2.5	YES	NO
EXP-5 PA58	Thick	14.350	54.0	12.0	39.0	>2.5	NO	NO	PS-3(04)	NO	14.409	202.0	42.0	44.8	>2.5	YES	NO
EXP-5 PA56	Thick	14.350	56.0	11.0	37.0	>2.5	NO	NO	EXP-2(360)	NO	14.409	205.0	22.2	35.5	>2.5	YES	NO
EXP-5 PA47	Thick	14.350	64.0	19.0	40.0	>2.5	NO	NO	EXP-4(02)	NO	14.409	207.0	22.9	54.4	>2.5	YES	0.3
EXP-5 PA50	Thick	14.350	65.0	26.0	41.0	>2.5	NO	NO	EXP-2(296)	NO	14.409	210.0	24.8	37.4	>2.5	NO	NO
EXP-5 PA48	Thick	14.350	78.0	31.0	37.0	>2.5	NO	NO	EXP-2(359)	NO	14.409	212.0	28.1	40.7	>2.5	YES	NO
EXP-5 PA55	Thick	14.350	82.0	17.0	64.0	>2.5	NO	0.8	EXP-2(358)	NO	14.409	213.0	21.6	34.9	>2.5	YES	NO
EXP-5 PA59	Thick	14.350	92.0	18.0	58.0	>2.5	NO	1.2	EXP-2(307)	NO	14.409	215.0	26.9	37.3	>2.5	NO	NO
EXP-5/1,4,7	Thick	14.350	95.0	13.1	44.4	>2.5	NO	NO	PS-3(03)	NO	14.409	216.0	42.4	43.6	>2.5	YES	NO

EXP-5 PA60	Thick	14.350	123.0	33.0	40.0	>2.5	NO	NO	PS/1988/OE	NO	14.409	217.6	33.8	51.3	0.7	NO	0.3
EXP-5 PA52	Thick	14.350	137.0	30.0	40.0	>2.5	NO	NO	PS-3(02)	NO	14.409	218.0	41.4	43.2	>2.5	YES	NO
EXP-5/1,4,7	Thick	14.350	148.0	34.8	55.7	>2.5	NO	NO	EXP-2(318)	NO	14.409	219.0	25.8	35.9	>2.5	NO	NO
EXP-5/OE	Thick	14.350	167.0	50.0	60.0	>2.5	NO	NO	PS-3(01)	NO	14.409	220.0	43.0	44.9	>2.5	YES	NO
EXP-5/2,5,8	Thick	14.350	192.0	41.0	50.0	>2.5	NO	NO	EXP-4(01)	NO	14.409	224.0	53.5	68.8	>2.5	YES	0.3
EXP-5/2,5,8	Thick	14.350	192.0	41.0	50.0	>2.5	NO	NO	EXP-2(357)	NO	14.409	225.0	21.9	34.7	>2.5	YES	NO
EXP-5 PA53	Thick	14.350	214.0	39.0	52.0	>2.5	NO	NO	EXP-2(347)	NO	14.409	231.0	24.6	36.4	>2.5	NO	NO
EXP-3/7000/01	Thick	14.346	100.0	39.0	66.0	>2.5	NO	NO	EXP-2(334)	NO	14.409	240.0	24.9	36.9	>2.5	NO	NO
EXP-4/2900/02	Thick	14.340	55.0	34.0	51.0	>2.5	NO	NO	EXP-2(331)	NO	14.409	243.0	24.8	36.2	>2.5	NO	NO
EXP-4 PA99	Thick	14.340	65.0	38.0	59.0	>2.5	NO	NO	EXP-2(328)	NO	14.409	256.0	24.5	34.7	>2.5	NO	NO
EXP-4 PA100	Thick	14.340	65.0	38.0	65.0	>2.5	NO	NO									

$$\frac{\partial C_{g,i}}{\partial t} = D_{AB}\frac{\partial^2 C_{g,i}}{\partial x^2} - \lambda_i C_{g,i} + R_{g,i} \tag{20}$$

The release rate of I_2 into the crack (molecules s^{-1}) can be evaluated from Fick's law of diffusion with the solution of the concentration profile in Eq. (20) for isotope *i*. The diffusion equation in Eq. (20) can be solved assuming a zero concentration for the initial condition, and a reflexive condition at the ends of the element and a zero concentration at the crack site (i.e., infinite sink) as shown in Fig. 8. Hence, with a crack at the mid-length location of the element:

$$R_{crack,i} = 2\left|D_{AB}\frac{\partial C_{g,i}}{\partial x}\right|_{x=0}\Rightarrow R_{crack,T} = \sum_{\text{all I isotopes}} R_{crack,i} \tag{21}$$

The second expression in Eq. (21) accounts for the total release of I_2 into the crack from all isotopes. The binary diffusion coefficient D_{AB} ($cm^2\ s^{-1}$) from Chapman–Enskog kinetic theory can be used for this analysis:

$$D_{AB} = 0.0018583\frac{\sqrt{T_g^3\left(\frac{1}{M_{He}}+\frac{1}{M_{I_2}}\right)}}{p\sigma_{AB}^2\Omega_{AB}} \sim .106\ \text{cm}^2\ \text{s}^{-1} \tag{22}$$

Here T_g is the gap temperature (~640 K), p is gap pressure (~10 atm or 1 MPa), $M_{He} = 4.003\ \text{g mol}^{-1}$, $M_{I_2} = 253.8\ \text{g mol}^{-1}$, σ_{AB} is the average collision diameter (3.78 Å), and Ω_{AB} is the collision integral (~1). Since the time constant for diffusion to the crack tip (i.e., for a sheath thickness $t_{clad} = 0.43$ mm) is:

$$\tau = t_{clad}^2/D_{AB} = (0.043\ \text{cm})^2/(0.106\ \text{cm}^2\ \text{s}^{-1}) = 0.02\ \text{s} \tag{23}$$

only axial diffusion in the gap need be considered as per Eq. (20).

3.3.4. Crack penetration time

As mentioned in Section 1, crack penetration requires the vaporization of ZrI_4 from the crack tip. Thus, assuming an instantaneous reaction at the crack tip, the release rate of predominantly ZrI_4 vapour is:

$$R_{Zr} = \frac{1}{2}R_{crack,T} \tag{24}$$

Hence, crack penetration occurs when the volume of the crack reaches a critical volume V_c at time t such that

$$\frac{\rho_{Zr}V_cN_A}{M_{Zr}} = \int_0^t R_{Zr}dt \tag{25}$$

where ρ_{Zr} the density of the Zircaloy sheath (6.5 g cm^{-3}), and M_{Zr} the molecular weight of Zr (91.2 g mol^{-1}). The critical crack volume V_c can be simplistically modelled as a right cylindrical cone, with a typical crack base width of $d_c \sim 5$ μm [32], and a crack length equal to the sheath thickness, i.e., $t_{clad} = 0.43$ mm. Hence, $V_c = \pi d_c^2 t_{clad}/12\ \text{cm}^3$ gives a critical volume of $\sim 2.8\times10^{-9}\ \text{cm}^3$. Substituting Eq. (24) into Eq. (25) and integrating provides a time t for crack breakthrough in the sheath when the critical volume is reached. This calculation may be somewhat conservative since instantaneous shear failure may occur through the remaining ~20% of the sheath thickness.

3.4. Model for oxide cracking/crack initiation

Rapid increases in fuel element power can produce high stress/strain levels in the sheathing, which can produce conditions suitable for a sheath chemical/mechanical failure. The effect of local stress concentration on a strain defect (i.e., mechanical overload) at sheathing circumferential ridges found at pellet interface positions during power increases has been previously analyzed

[33,34]. This analysis shows that there is a correspondence between mechanical stress concentrations causing mechanical failure and experimental power-ramp failure probabilities, thus indicating the threshold required for oxide cracking and crack initiation [33].

Extensive experimental observations for CANDU fuel show that defect probabilities can be related to critical values of the ramped power P_c (in kW/m), power increase ΔP_c (in kW/m), and dwell time t_{dwell} (in h) at the ramped power level for a given burnup w (in MW h/kg U) [35]:

$$P_c = 44.6 + (232/w) - 22[0.5 - \exp(-2.3t_{dwell})] \quad (26a)$$

$$\Delta P_c = 6 + (1460/w) - 24[0.5 - \exp(-2.3t_{dwell})] \quad (26b)$$

Moreover, for a typical dwell time of t_{dwell} = 0.3 h (1080 s) [33,35], Eqs. (26a) and (26b) reduce to:

$$P_c = 44.6 + (232/w) \quad (27a)$$

$$\Delta P_c = 6 + (1460/w) \quad (27b)$$

Probability curves have in fact been developed for this representative dwell time, such that when a power ramp occurs (i.e., $\Delta P > 0$), there is a chance of failure depending on the thickness of the CANLUB protective coating [35]. In particular, based on several selected power ramp cases in Table 2, failure is predicted for a given CANLUB thickness when both of the following conditions are met: (i) with no CANLUB, $(P - P_c) \geqslant 0$ kW/m and $(\Delta P - \Delta P_c) \geqslant 1.4$ kW/m; (ii) for a "thin" layer of CANLUB thickness of ~2.5 μm, $(P - P_c) \geqslant 0$ kW/m and $(\Delta P - \Delta P_c) \geqslant 2.2$ kW/m; (iii) and for a "thick" interlayer coating of ~5 μm, $(P - P_c) \geqslant 3.3$ kW/m and $(\Delta P - \Delta P_c) \geqslant 6.8$ kW/m [35]. The CANLUB coating helps to inhibit SCC failure. Hence, ξ_{free} can be taken as unity if both conditions are high enough to exceed the threshold condition (or is zero otherwise) with a sufficient dwell time (t_{dwell} = 1080 s) for crack initiation to occur. At this point, chemical effects now become important for crack penetration and propagation, which can lead to element failure (i.e., sheath breakthrough) if there is a sufficient supply of volatile iodine as determined in Section 3.3 based on the given element power history.

This model was extensively tested against an available database of power ramp experience from commercial power stations (PS) (172 cases) and experimental irradiations (EXP) (163 cases) as shown in Table 3 [36,37]. The oxide cracking model was found to predict failure for 70% of all cases and 77% of the power reactor cases.

4. Discussion

4.1. Model benchmarking

The resultant model in Section 3 was implemented into the COMSOL Multiphysics software platform in order to benchmark the model against power ramp experiments.

An experimental program with defective CANDU-type fuel elements was carried out at the Chalk River Laboratories (CRL) [38]. Failed elements, with various degrees of sheath damage, were irradiated in separate tests in the X-2 experimental loop at the National Research Experimental (NRX) reactor. Experiment FFO-104 was a well-controlled in-reactor experiment that represented a power-ramp failure, which can be explicitly used to benchmark the SCC model. The fuel element was irradiated to 240 MW h kg U^{-1} in an earlier irradiation at 30 kW m^{-1}. A pre-conditioning period of 30 kW m^{-1} was then undertaken in order to restore the short-lived fission product inventory, where the element reached a fuel burnup of 278 MW h kg U^{-1}. This latter irradiation period was immediately followed by a power ramp to 58 kW m^{-1} (see Fig. 7).

For this simulation, a typical crack initiation time of t_{dwell} = 1080 s was assumed (see Section 3.4) after which time ξ_{free} was set equal to unity to initiate the chemical attack of the Zircaloy sheathing for crack propagation. The mechanistic COMSOL simulation indicated that crack penetration in Eq. (25) would occur quickly after this time by iodine vapour transport within ~2 min principally due to the availability of the long-lived iodine inventory that was established during the previous irradiation history (Fig. 7). Hence, the failure time taken from the start of the power ramp was predicted to be ~20 min, which is in excellent agreement with that observed (i.e., ~20 min).

Thus, the current model appears to appropriately model the underlying chemical phenomena after crack initiation. This simulation indicates that the major time to failure is due primarily to the time required to expose the bare Zr surface normally covered by a

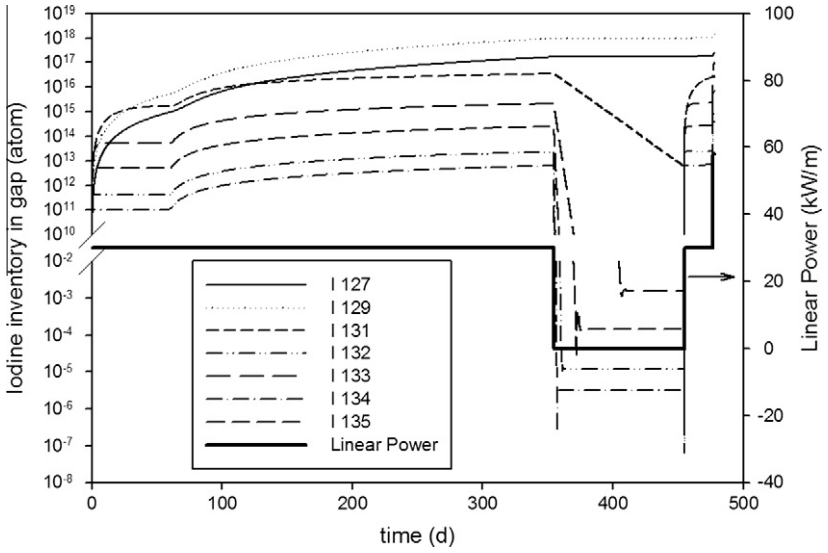

Fig. 7. Inventory of short and long-lived iodine isotopes in the gap during the FFO-104 irradiation. The element linear power is also shown.

protective oxide and crack initiation rather than from crack propagation (due to chemical iodine vapour transport). As shown in Table 3, the overall failure times were predicted within a factor of 4 for 91% of the observed cases.

4.2. Proposed mitigation strategies for I-SCC

Based on this thermodynamic and kinetic analysis, a possible mitigation strategy is further proposed in this work. This strategy includes supplementing alkali metal additives to the CANLUB coating (Section 4.2.1) and/or altering the conventional sintering processes (Section 4.2.2).

4.2.1. Alkali metal additives to CANLUB

As mentioned previously, CANLUB appears to act as a getter for iodine, despite the fact that carbon and iodine do not react. Impurities in the CANLUB are thought to have an important role in CANLUB effectiveness. Adding cesium-based compounds in the CANLUB could provide a higher concentration of species that could bind with iodine, or other corrosive agents like ZrI_4, residing in the fuel-to-sheath gap. The CANLUB layer would retain the corrosive species (I) through adsorption and absorption processes, preventing them from reaching the Zircaloy sheath and initiating or proliferating cracks. Hence, the employment of Cs- (or other alkali metals, Na-, K-, Rb-) containing compounds at low concentrations like Cs_2O, Cs_2ZrO_3, Cs_2CO_3, etc., are expected to have a suppressing effect on I-SCC.

Laboratory experiments show that CsI does not cause SCC in the absence of radiation, and metallic Cs and Cs_2O will suppress I-SCC [7], in accordance with the following reaction

$$I_{2(g)} + Cs_2O_{(s)} = 2CsI_{(g)} + 1/2O_{2(g)} \quad \Delta G^\circ = -533 \text{ kJ at } 600 \text{ K} \tag{28}$$

Cs_2O will preferentially react with free iodine to produce CsI in a vapour. As a result, the iodine will not be available to react with the zirconium metal. However, the effect of fission fragment radiolysis to liberate Cs as a corrosive product needs testing in a radiation field. Iodine reacting with cesium oxide compounds also has the effect of concurrently releasing oxygen, which would likely combine with any exposed zirconium metal. The general belief is that oxygen suppresses I-SCC by the passivity associated with the ZrO_2 layer.

Cs-based CANLUB additives, if present in sufficient quantity during burnup, may therefore have added beneficial effects. This speculation merits experimental exploration and confirmation, particularly since it does not introduce a foreign element.

4.2.2. Alteration to the conventional sintering process

Only when the ZrO_2 layer is cracked, or degraded, is the iodine capable of initiating attack of the Zircaloy sheath. In one of the final steps of the sintering process for UO_2 fuel, the fuel pellets are exposed to H_2 gas in a furnace at a high temperature (~2073 K). Hydrogen reacts with any oxidized UO_2 giving the overall result of a stoichiometric $UO_{2.000}$ fuel pellet:

$$UO_{2+x} + xH_2 \rightarrow UO_2 + xH_2O \tag{29}$$

An alternative proposed remedy would alter this final step in the process by exposing the pellets to a small partial pressure of O_2, oxidizing slightly the outer surface (only) of dense (nearly pore free) fuel pellets. To accomplish this, the hydrogen is proposed to be passed through water prior to entering the furnace, thereby

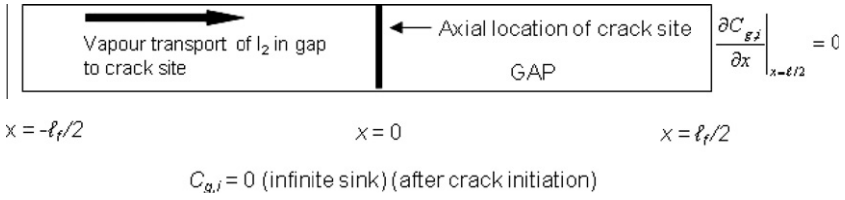

Fig. 8. Schematic for the diffusion of iodine in the gap to the crack site.

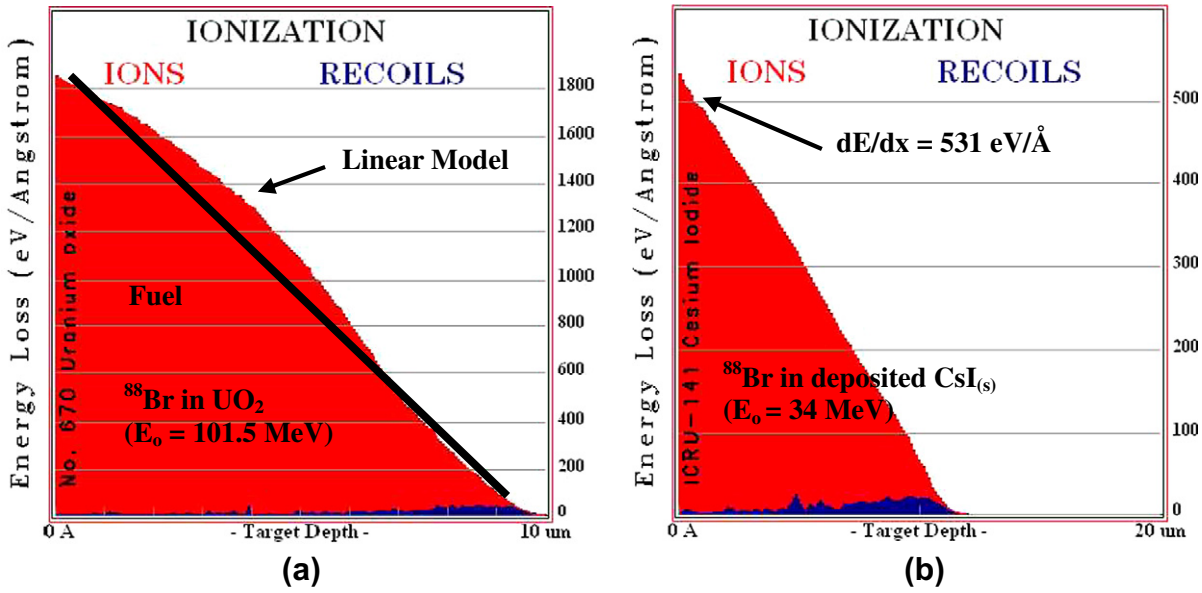

Fig. 9. Energy loss of the fission fragment ^{88}Br in (a) UO_2 fuel and (b) in the CsI deposit.

introducing water vapour at a concentration determined by the water temperature. The oxidation is controlled by the H_2O/H_2 ratio of gases in the furnace. The partial pressure of oxygen relates to the H_2O/H_2 ratio by the equilibrium constant of the following equilibrium:

$$2H_2 + O_2 \rightarrow 2H_2O \tag{30}$$

The equilibrium constant is written in terms of the H_2O/H_2 partial pressure ratio and the partial pressure of oxygen as follows:

$$K_{Eq} = \left(\frac{P_{H_2O}}{P_{H_2}}\right)^2 \cdot \frac{1}{P_{O_2}} \tag{31}$$

Only the ratio of H_2O/H_2 is significant in determining P_{O_2} at a given sintering (oxidation) temperature because the H_2 gas being humidified could be diluted in argon so the gas would not have to be excessively humidified. The exposure of the pellets to a small partial pressure of oxygen would slightly oxidize the pellets creating a controlled and very thin layer of UO_{2+x} [39]. This layer is sufficiently thin to maintain the overall stoichiometry of the fuel pellet near $UO_{2.000}$. However, the diffuse layer is sufficient to release enough oxygen to continually repair the protective oxide layer on the sheath, should this be damaged or breached by pellet/sheath contact. To determine if the above scenario is sound, experiments and numerical model construction must be undertaken to test the kinetics of the reactions in Eqs. (29) and (30), which are currently being planned at the Atomic Energy of Canada Limited–Chalk River Laboratories (AECL–CRL).

5. Conclusions

1. In order to model the phenomena of iodine-induced stress corrosion cracking, a thermodynamic analysis was carried out to better understand the iodine chemistry in the fuel-to-sheath gap. This analysis was utilized to advance the development of an I-SCC mechanistic kinetic model for fuel sheathing. The treatment incorporated fission-product diffusion through the fuel matrix, fission fragment radiolysis, I_2 vapour transport in the fuel-to-sheath gap, and crack propagation by ZrI_4 production. The governing differential equations of the model were numerically solved within the COMSOL Multiphysics® platform. The SCC model was benchmarked against a well-characterized experiment that investigated power ramp behaviour in the X-2 defect loop facility at AECL–CRL. The model was in good agreement with the observations for this experiment. Further model validation requires power-ramp reactor experience.
2. A possible remedy for SCC phenomena is suggested which includes: (i) the addition of alkali metal–oxygen containing additives to the CANLUB coating to getter the chemically-reactive iodine; and (ii) the slight oxidation of the fuel pellets (surface layer) in the manufacturing process to provide a source of oxygen for maintenance and repair of the protective oxide layer. Experiments to test these ideas are in the process of being initiated by AECL–CRL.

Acknowledgements

The authors wish to thank J. Hood of the Candesco Research Corporation, and R. Ham-Su, B. Surette, and D. Barber of AECL–CRL for their assistance and advice. This work was sponsored by University Network of Excellence in Nuclear Engineering (UNENE), CANDU Owners Group (COG) and Natural Sciences and Engineering Research Council of Canada (NSERC) as part of the Industrial Research Chair program in Nuclear Fuel at the Royal Military College of Canada.

Appendix A. SRIM analyses

The fission fragment range (μ) for the recoil model can be evaluated with an SRIM (Stopping and Range of Ions in Matter) code analysis [40]. This analysis can also be used to determine the energy loss in the CsI deposits (dE/dx). The energy loss in UO_2 fuel of density 10.7 g cm^{-3} is evaluated in Fig. 9a and Fig. 10a for the ^{88}Br and ^{135}I fission fragments, respectively, assuming initial energies E_o of 101.5 MeV and 66.6 MeV for these light and heavy products [27]. Hence, the calculated ranges of the fission fragments in the fuel (μ_{Br} = 8.9 μm and μ_I = 6.4 μm) yield an average value μ = 7.7 μm.

The average energy of the given fission fragment (Br or I) leaving the fuel surface follows from the energy loss curves in Fig. 9a and Fig. 10a, which can be approximated as straight lines:

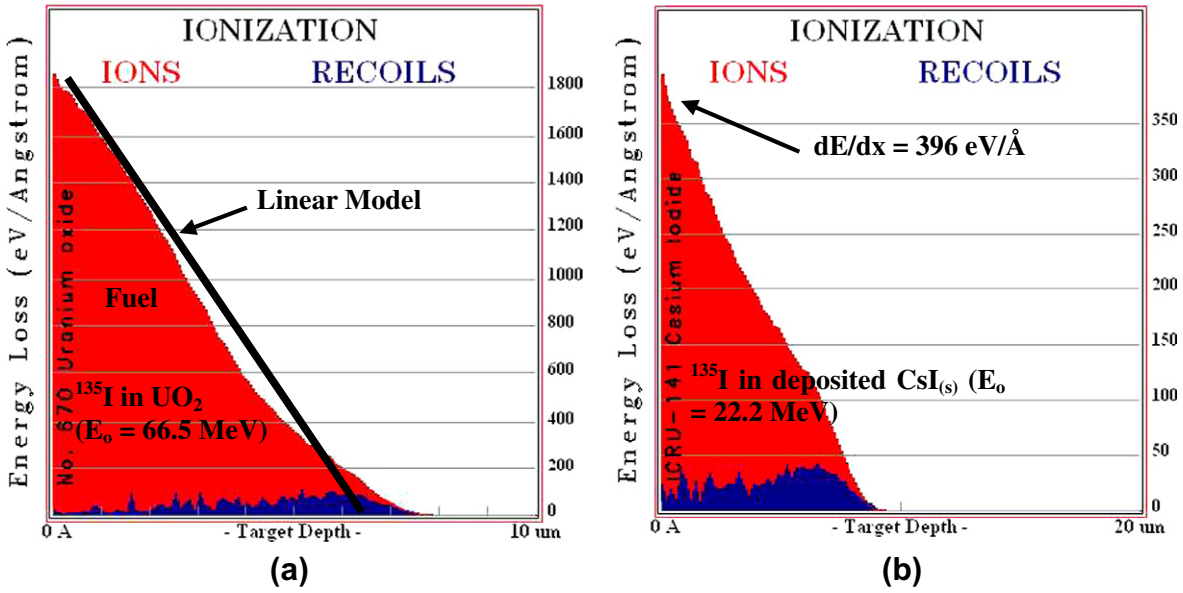

Fig. 10. Energy loss of the fission fragment ^{135}I in (a) UO_2 fuel and (b) in the CsI deposit.

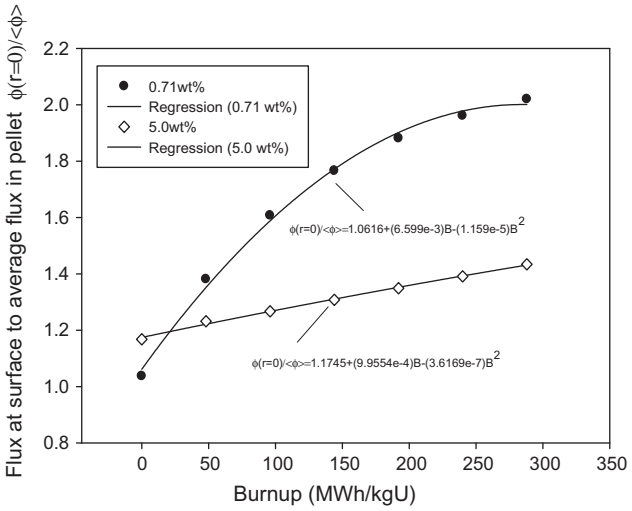

Fig. 11. Graph of the ratio of surface flux to average flux in a pellet versus burnup B (in MW h/kg U) to determine the flux depression factor for various enrichments of ^{235}U.

$$\frac{dE}{dx} \sim \left(\frac{-2E_o}{\mu}\right)\left(1-\frac{x}{\mu}\right) \tag{A-1}$$

Eq. (A-1) can be subsequently integrated to yield the particle energy as a function of distance x from the fuel surface:

$$E(x) = E_o\left[1-\frac{x}{\mu}\right]^2 \tag{A-2}$$

Hence, as expected when $x = \mu$, $E(\mu) = 0$ and when $x = 0$, $E = E_o$. The average energy for a fission fragment leaving the fuel surface is the expectation value:

$$\langle E\rangle = \int_0^{\mu} E(x)dx \Big/ \int_0^{\mu} dx \tag{A-3}$$

Thus, substituting in Eq. (A-2) into Eq. (A-3) and integrating, yields

$$\langle E\rangle = E_o/3 \tag{A-4}$$

The bromine and iodine fission fragments will therefore have an average energy of ~34 MeV and 22 MeV, respectively, as they traverse through the thin CsI deposit of thickness Δx and density of 4.5 g cm^{-3}. Since this deposit has a thickness on the order of angstroms, the energy loss value dE/dx can be taken as the value near the top of the curves of Figs. 9b and 10b, e.g., $dE/dx \sim 531$ eV/Å for ^{88}Br and $dE/dx = 396$ eV/Å for ^{135}I, yielding an average value of $dE/dx \sim 464$ eV/Å.

Appendix B. Calculation of flux depression factor ξ_{skin}

The thermal neutron flux, accounting for the plutonium build-up on the surface of the fuel pellet as a function of the UO_2 fuel pellet radius r is [41]:

$$\phi(r) = \phi(0)\{I_o(\kappa r) + \beta e^{(\lambda(r-a))}\} \tag{B-1}$$

where β, λ, and κ are coefficients for a specific fuel burnup β, ^{235}U enrichment, and radius a. The flux depression factor, ξ_{skin}, in Eq. (13) can therefore be derived using the flux depression tables for β, λ, and κ [41]. The volumetrically-averaged thermal neutron flux in the fuel $\langle\phi\rangle$ can be determined by estimating the volumetrically-averaged flux in the fuel stack of length ℓ for a pellet of radius a [42]:

$$\langle\phi\rangle = \frac{2\pi\ell\int_0^a r\phi(r)dr}{\pi a^2\ell} \tag{B-2}$$

Thus, evaluating Eq. (B-1) at $r = a$ and dividing it by Eq. (B-2), yields the ratio of the thermal neutron flux at the UO_2 fuel surface $\phi(r = a)$ to the volumetrically-averaged thermal neutron flux in the UO_2 fuel $\langle\phi\rangle$, yielding the Pu-enhanced factor ξ_{skin}

$$\xi_{skin} = \frac{\phi(r=a)}{\langle\phi\rangle} = \frac{1}{2}\frac{\kappa a^2\lambda^2\{I_o(a\kappa)+\beta\}}{a\lambda^2 I_1(a\kappa)+\beta\kappa e^{-a\lambda}+a\beta\kappa\lambda-\beta\kappa} \tag{B-3}$$

Fig. 11 shows the relationship of ξ_{skin} for different UO_2 fuel enrichments. The sweep gas experiments used 5 wt.% enriched fuel, whereas CANDU fuel is naturally-enriched at 0.71 wt.%.

References

[1] S.A. Nikulin, A.B. Rozhnov, Corrosion 47 (1–2) (2005).
[2] R. Ham-Su, Atomic Energy of Canada Limited, Private Communication, October 2009.
[3] N. Marchal, C. Campos, C. Garnier, Comput. Mater. Sci. 45 (2009) 821–826.
[4] K. Edsinger, K.L. Murty, J. Mater. (July) (2001) 9–13.
[5] M. Tayal, A. Sun, M. Gaces, P. Reid, P. Fehrenbach, B. Surette, E. Suk, Mechanism for power ramp failures in CANDU fuel, in: Tenth International Conference on CANDU Fuel, Canadian Nuclear Society, Ottawa, Canada, October 5–8, 2008.
[6] S.A. Nikulin, A.B. Rozhnov, Corrosion 47 (9–10) (2005).
[7] P.S. Sidky, J. Nucl. Mater. 256 (1998) 1–17.
[8] T. Do, K.G. Irving, W.H. Hocking, J. Nucl. Mater. 383 (2008) 34–40.
[9] J.C. Wood, J.R. Kelm, Res. Mech. 8 (1983) 127–161.
[10] S.B. Farina, Corrosion 61 (9) (2005) 847–856.
[11] I. Schuster, C. Lemaignan, J. Joseph, Nucl. Eng. Des. 156 (1995) 343–349.
[12] P. Jacques, F. Lefebve, C. Lemaignan, J. Nucl. Mater. 264 (1999) 239–248.
[13] M. Fregonese, C. Olagnon, N. Godin, A. Hamel, T. Douillard, J. Nucl. Mater. 373 (2008) 59–70.
[14] S.Y. Park, J.H. Kim, M.H. Lee, Y.H. Jeong, J. Nucl. Mater. 376 (2008) 98–107.
[15] K. Konashi, Y. Shiokaw, H. Kayano, J. Nucl. Mater. 232 (1996) 181–185.
[16] S.Y. Park, B.K. Choie, J.Y. Park, Y.H. Jeong, Effect of hydride on the ISCC crack initiation and propagation in the high burnup-simulated nuclear fuel cladding, in: Proceeding of Top Fuel, Paper 2074, 2009.
[17] M.B. Theodore, T.B. Lindemer, Nucl. Technol. 40 (1978) 297–305.
[18] W.T. Thompson, B.J. Lewis, E.C. Corcoran, M.H. Kaye, S.J. Whie, F. Akbari, Z. He, R. Verrall, J.D. Higgs, D.M. Thompson, T.M. Besmann, S.C. Vogel, Int. J. Mater. Res. 98 (2007) 10.
[19] E.H.P. Cordfunke, R.J.M. Konings, Thermochemical Data for Reactor Materials and Fission Products, Elsevier Science Publishers B.V., North Holland, 1990.
[20] M. Kleczek, Thermodynamic and Kinetic Modelling of Iodine Induced Stress Corrosion Cracking in Nuclear Fuel Sheathing, MASc Thesis, April 2010.
[21] A.H. Booth, A Suggested Method for Calculating the Diffusion of Radioactive Rare Gas Fission Products from UO_2 Fuel Elements and a Discussion of Proposed In-Reactor Experiments that may be Used to Test Its Validity, Atomic Energy of Canada Limited, AECL-700, 1957.
[22] G.V. Kidson, J. Nucl. Mater. 88 (1980) 299–308.
[23] S.D. Beck, The Diffusion of Radioactive Fission Products from Porous Fuel Elements, USAEC Report BMI – 1433, April 1960.
[24] B.J. Lewis, J. Nucl. Mater. 172 (1990) 197–205.
[25] B.J. Lewis, A. El-Jaby, J. Higgs, W.T. Thompson, F.C. Iglesias, R. Laidler, J. Armstrong, R. Stone, R. Oduntan, J. Nucl. Mater. 366 (2007) 37–51.
[26] B.J. Lewis, R.J. Green, C.W.T. Che, Nucl. Technol. 98 (1992) 307–321.
[27] B.J. Lewis, J. Nucl. Mater. 148 (1987) 28.
[28] C. Wise, J. Nucl. Mater. 152 (1988) 102.
[29] D.R. Olander, Fundamental Aspects of Nuclear Reactor Fuel Elements, Energy Research and Development Administration, US Department of Commerce, Report TID-26711 Pt. 1, 1976.
[30] R.M. Horton, R.L. Kinney, The kinetics of formation of ZrI_4 from Zr and I_2, Report No. IRN15683758, Electrothermics and Metallurgy and Corrosion Divisions, Electrochemical Society, 1975, p. 317.
[31] A. Soba, A. Denis, Nucl. Eng. Des. 238 (2008) 3292–3298.
[32] B. Cox, B.A. Surette, J.C. Wood, J. Nucl. Mater. 138 (1986) 89–98.
[33] H.E. Sills, Cladding Performance during Power Changes, Atomic Energy of Canada Limited Report AECL-5908, December 1977.
[34] J.H. Gittus, TRG Report 1547 (S), 1968.
[35] W.J. Penn, R.K. Lo, J.C. Wood, Nucl. Technol. 34 (1977) 249–268.
[36] T.J. Carter, Nucl. Technol. 45 (1979) 166.
[37] E. Mizzan, J. Novac, Private Communication.
[38] B.J. Lewis, R.D. MacDonald, N.V. Ivanoff, F.C. Iglesias, Nucl. Technol. 103 (1993) 220–245.
[39] M. Moalem, D.R. Olander, J. Nucl. Mater. 182 (1991) 170–194.
[40] J.F. Ziegler, J.P. Biersack, U. Littmark, The Stopping and Range of Ions in Solids, Pergamon Press, New York, 1985.
[41] M.J.F. Notley, Nucl. Technol. 44 (1979) 445.
[42] A. El-Jaby, A Model for Predicting Coolant Activity Behaviour for Fuel-Failure Monitoring Analysis, PhD Thesis, Royal Military College of Canada, 2009.
[43] D.B. Knight, Application of the ANS5.4 Fission Product Release Model to CANDU Fuel, MASc Thesis, Royal Military College, 1990.